



Supplementary Materials for  
**Reversible structural transformations in supercooled liquid water  
from 135 to 245 K**

Loni Kringle\*, Wyatt A. Thornley\*, Bruce D. Kay†, Greg A. Kimmel†

\*These authors contributed equally to this work.

†Corresponding author. Email: gregory.kimmel@pnnl.gov (G.A.K.); bruce.kay@pnnl.gov (B.D.K.)

Published 18 September 2020, *Science* **369**, 1490 (2020)  
DOI: 10.1126/science.abb7542

**This PDF file includes:**

Materials and Methods  
Supplementary Text  
Figs. S1 to S17  
References

## Materials and Methods

### Nanoscale water films

Amorphous solid water (ASW) films were vapor deposited onto the substrate under ultrahigh vacuum ( $\sim 10^{-10}$  torr) at 70 K using a calibrated molecular beam source. A Pt(111) single crystal or a graphene layer on Pt(111) were used as substrates. The water films were 6 mm in diameter and a few nanometers thick. For the results shown in Figures 1 – 4, the water coverages were 50 monolayers (ML), where  $1 \text{ ML} \equiv 1.0 \times 10^{19} \text{ H}_2\text{O}/\text{m}^2$ . The thicknesses of the films were not measured but were presumed to change due to changes in the density of water as a function of temperature. For a nominal density of  $1 \text{ g}/\text{cm}^3$ , a 50 ML film is 15 nm thick.

### Transient heating with nanosecond laser pulses

The pulsed heating method has been described in detail previously (35, 36). Briefly, laser pulses from a Nd-YAG laser ( $\lambda = 1,064 \text{ nm}$ ,  $1 - 5 \text{ Hz}$ , pulse width  $\sim 10 \text{ ns}$ ) transiently heat the near-surface region of the metal substrate and the adsorbed water films to a maximum temperature,  $T_{max}$ . Rapid diffusion of heat deeper into the substrate quickly cools the adsorbed water layers and results in maximum heating and cooling rates of  $\sim 2 \times 10^{10}$  and  $\sim 5 \times 10^9 \text{ K/s}$ , respectively. As an example, Fig. S13 shows  $T(t)$  for  $T_{max} = 223 \text{ K}$  and  $T_{measure} = 70 \text{ K}$  (solid black line). For any individual experiment,  $T(t)$ , and its corresponding  $T_{max}$  are set by choosing the energy per pulse for the laser,  $E_p$ . As a result,  $T_{max}$  can be reliably set over a wide range of temperatures.

As discussed in our earlier report (35), the desorption of crystalline ice during pulsed heating was used to determine  $T_{max}$  as function of laser pulse energy. The absolute uncertainty in the overall temperature calibration is estimated to be  $\pm 3 \text{ K}$  for the temperature range shown in Figure 4 (i.e. corresponding to a potential temperature shift of the entire data set of  $\pm 3 \text{ K}$ ). For

each individual experiment at a particular  $T_{max}$  (e.g. Figure 2), uncertainty in setting  $E_p$  and subsequent drift in the laser pulse energy (at the level of  $\sim 1\%$ ) lead to small temperature differences of up to  $\pm 1.5$  K between experiments at the same nominal  $T_{max}$ . In addition, the optical setup was designed to produce a “flat-top” laser pulse profile (i.e. a constant lateral intensity) that had a larger diameter than the water film such that the same temperatures versus time were obtained across the entire water film. Nonetheless, small deviations from an ideal “flat-top” beam profile lead to lateral variations in  $T_{max}$  of approximately  $\pm 4$  K for  $190 \text{ K} \leq T_{max} \leq 240 \text{ K}$ . For the results shown in Figure 4, calculations show that accounting for these lateral temperature variations would lead to a slightly narrower range of temperatures for the transition of  $f_{HQW}^{SS}$  from  $\sim 0$  to  $\sim 1$  (e.g.  $\Delta T \sim 8.2$  K instead of 8.5 K in the logistic function fit to the data). Despite the experimental uncertainties, a key point is that the range of temperatures explored in these experiments, which is set by  $E_p$ , is large. Furthermore, because  $E_p$  could be set to  $\pm 1\%$ , the temperature jump associated with the heat pulse was also controlled to approximately  $\pm 1\%$ .

For the experiments reported here  $T_{measure}$  was 70 K, while our earlier reports (24, 33, 35, 36) used  $T_{measure} = 90$  K.  $T_{measure} = 70$  K was chosen for the current experiments because HQW undergoes some slow structural relaxation (towards LDA) at 90 K that interfered with longer-duration experiments (e.g.  $\sim 0.5$  day), such as those following the evolution of HQW for  $T_{max} < 200$  K (see e.g. Fig S8). For comparison, Figure S13 shows the calculated  $T(t)$  for  $T_{max} = 223$  K and  $T_{measure} = 90$  K (black dashed line). Due to the lower starting temperature used here, higher laser pulse energies were required to reach the same maximum temperature,  $T_{max}$ . Also, for a given  $T_{max}$  and a lower  $T_{measure}$ , the heating rates and cooling rates are slightly larger before and after  $T_{max}$ , respectively. These differences in the heat pulse,  $T(t)$  are accounted for in the temperature calibration procedure, but otherwise had no effect on the results reported here.

For experiments with shorter laser pulses, the pressure within the heated region can increase prior to thermal expansion of the material (see e.g. (37)). The timescale for thermal expansion,  $t_{exp}$ , is set by the characteristic length scale,  $L$ , and the speed of sound,  $v$ , in the material:  $t_{exp} = L/v$ . After thermal expansion, the system is in hydrodynamic equilibrium. For these experiments, the thickness of the films ( $\sim 15$  nm) is the relevant length and the speed of sound is  $\sim 1500$  m/s. Therefore, the characteristic time for thermal expansion for the 15 nm thick films is  $\sim 1 \times 10^{-11}$  s. During this short time, the temperature changes less than 1 K even on the most rapid part of the heat ramp. As a result, the system remains essentially in hydrodynamic equilibrium at ambient pressure throughout the heat pulse.

#### Infrared reflection absorption spectroscopy

All the IR spectra were acquired at 70 K after a given number of heat pulses,  $N_p$ . The typical spectra had 500 scans of the Fourier-transform infrared (FTIR) spectrometer (Bruker, Vertex 70) and were collected at a resolution of  $4$   $\text{cm}^{-1}$ . Because of the substantial differences in the band shape for isolated HOD in  $\text{H}_2\text{O}$  for crystalline ice and liquid water, water with  $\sim 10\%$  HOD in  $\text{H}_2\text{O}$  was used to increase the sensitivity for detecting the onset of crystallization. Infrared absorption reflection spectroscopy (IRAS) was used to monitor the changes in local structure, as evidenced by spectral changes in the OH stretching region ( $\sim 3000 - 3700$   $\text{cm}^{-1}$ ) and the isolated HOD stretch region ( $\sim 2350 - 2500$   $\text{cm}^{-1}$ ). ASW films deposited at 70 K have IR spectra that are similar to HQW (see Fig. S14). However, for deposition at higher temperatures, the IR spectra of the ASW films increasingly resemble the spectrum for LDA as some annealing occurs during the deposition. For example, a film deposited at 115 K is quite similar to LDA (see Fig. S14). Note that for our setup, dosing at temperatures above  $\sim 115$  K led to increasing amounts of crystalline

ice within the as-deposited films. For the results presented here (except for Fig. S14), the ASW films were deposited at 70 K and were always converted to either LDA or HQW to begin the experiments. We note that ASW films deposited at 70 K resulted in the same steady-state configurations versus  $T_{max}$  and had similar relaxation kinetics to those observed for HQW.

### Relationship between pulse-integrated and instantaneous measurements

For transient heating experiments, the change in some temperature-dependent process (e.g. desorption, structural relaxation, crystallization, etc.) produced by a single heat pulse is given by the integral of an instantaneous rate,  $R(T)$ , over the laser-induced heat pulse,

$$\tilde{R}(T_{max}) = \int_{pulse} R(T(t)) dt. \quad (S1)$$

Setting the laser pulse energy determines  $T(t)$  and the maximum temperature  $T_{max}$ . (In the text, we use  $T_{max}$  as a shorthand to refer to entire heat pulse,  $T(t)$ .) We have previously characterized in detail the heat pulses,  $T(t)$ , for thin water films adsorbed on Pt(111) and graphene/Pt(111) versus the laser pulse energy (35).

For the results presented here, the main processes of interest are the structural relaxation rate,  $R_{relax}(T)$ , and crystallization kinetics of the water films (which depends on the ice nucleation and growth rates,  $J(T)$  and  $G(T)$ , respectively). Note that because equation S1 is an integral equation, there is not a unique inversion to determine  $R(T)$  from a finite number of measurements of  $\tilde{R}(T_{max})$ . In practice, the processes of interest are typically smoothly varying functions of temperature such that this issue is not a significant problem. A key point is that for any process where the rate increases rapidly with temperature,  $\tilde{R}(T_{max})$  will be largely determined by  $R(T_{max})$ . Figure S13 shows an example of the instantaneous rate versus time during a heat pulse where  $R(T)$  is assumed to have an Arrhenius form,  $R(T) = R_0 e^{-E_a/k_b T}$ . As seen in the figure,

$R(T)$  is sharply peaked around  $T_{max}$ . Furthermore,  $T_{measure}$  is chosen such that  $R(T_{measure})$  is small enough that the observed changes result from the heat pulses and are not occurring during the (relatively long) time between heat pulses when the sample is at  $T_{measure}$ . In that case, the evolution of the system occurs in a series of discrete steps associated with the individual heat pulses.

#### Procedure for determining $f_{LDA}$ , $f_{HQW}$ , and $f_{CI}$ from the IR spectra

For water heated to  $T_{max}$  for  $N_p$  heat pulses,  $f_{LDA}(T_{max}, N_p)$ ,  $f_{HQW}(T_{max}, N_p)$ , and  $f_{CI}(T_{max}, N_p)$  were determined by fitting the IR spectrum to a linear combination of reference spectra for LDA, HQW and CI. As described in the main text, LDA was prepared by annealing the water at 135 K for 130 s. Note that changing the annealing temperature by  $\pm 5$  K, or the annealing time from 50 to 500 s, led to essentially indistinguishable spectra for the LDA. The HQW was prepared by transiently heating a film to  $T_{max} = 297$  K, typically for 3 heat pulses. As shown in Figure S9, any pulsed heating temperature above  $\sim 246$  K produces water films with the same hyper-quenched structure as indicated by the (indistinguishable) IR spectra. The CI spectra were obtained from films that had been crystallized by pulsed heating. For the results shown in the main text, the crystalline fraction,  $f_{CI}$ , was small (i.e.  $\leq 0.02$  except for  $N_p > 500$  in Fig. 3B). In that case,  $f_{LDA}$  and  $f_{HQW}$  are simply related to each other:  $f_{LDA} + f_{HQW} \approx 1$ . Fig. S6 shows several spectra along with the results of the fitting procedure. In these examples, the crystalline component of the fitting was  $\leq 0.02$  and is omitted for clarity. The top and middle rows of the figure show several “steady-state” spectra (orange lines), the results of the fitting procedure (black dashed lined), and the scaled LDA (blue line) and HQW (red line) components. The bottom row in Fig. S6 shows

several spectra and the resulting fit for an HQW film that was heated to 190 K after various numbers of heat pulses.

The steady state fraction of HQW,  $f_{HQW}^{SS}(T_{max})$ , was determined by two methods. In the first approach,  $f_{HQW}^{SS}(T_{max})_i$  for an experiment (where the subscript  $i$  refers to an individual experiment) was determined from the average of the values of  $f_{HQW}(T_{max}, N_p)$  for several spectra just prior to crystallization.  $f_{HQW}^{SS}(T_{max})$  was then found by averaging over all the individual experiments at a given temperature:  $f_{HQW}^{SS}(T_{max}) = \frac{1}{N} \sum_{i=1}^N f_{HQW}^{SS}(T_{max})_i$ . In the second approach,  $f_{HQW}(T_{max}, N_p)$  was fit to a stretched exponential function

$$f_{HQW}(N_p, T_{max}) = f_{HQW}^{SS}(T_{max}) + (1 - f_{HQW}^{SS}(T_{max})) \cdot \exp((-N_p/N_r)^\beta), \quad (S2)$$

where  $N_r$  is the characteristic number of pulses to relax the structure, and  $f_{HQW}^{SS}(T_{max})_i$  was taken as  $f_{HQW}(T_{max}, N_p \rightarrow \infty)$ . The values of  $f_{HQW}^{SS}(T_{max})$  determined from the two procedures were the same within the experimental uncertainty (see error bars in Figure 4).

### Relationship of current experiments to previous reports

Previously, we used the pulsed-heating technique to investigate the growth rate,  $G(T)$ , of crystalline ice (CI) in thin water layers (~7 nm thick) adsorbed on CI templates versus temperature for  $180 \text{ K} < T_{max} < 262 \text{ K}$  (24). The liquid diffusivity,  $D(T)$ , was then obtained by using the Wilson-Frenkel model of crystal growth kinetics. The presence of the CI template led to prompt crystallization of the water layer upon pulsed heating. In contrast, in this study, the water layers initially contain no ice, which allowed us to investigate how the structure of supercooled water depends on temperature prior to the onset of appreciable, irreversible crystallization.

## Supplementary Text

### A. Bulk water versus thin films

Because the structure of water at interfaces converges to the bulk within  $\sim 3 - 4$  monolayers (38, 39), most of the water experienced a bulk environment. For water films on both Pt(111) and graphene/Pt(111),  $f_{HQW}^{SS}(T_{max})$  was the same within experimental error (Fig. S7) suggesting that the substrate did not play a significant role. Capping the water films with a decane layer also did not appreciably change the results (Fig. S15). The structural evolution versus the number of heat pulses in water films with coverages from 25 to 100 ML was also similar. The water films were flat, so the internal pressure was not raised due to curvature effects. The disjoining pressure,  $P_D$ , within these films was also small. The classical disjoining pressure is given by,  $P_D = -A_H/(6\pi\delta^3)$ , where  $A_H$  is the Hamaker constant and  $\delta$  is the film thickness (40). For water films on gold,  $A_H$  is  $\sim 4 \times 10^{-19}$  J (41), which gives a disjoining pressure of  $6.3 \times 10^3$  Pa or  $\sim 0.06$  atmospheres for 15 nm films. The pressure for water on a platinum substrate should not be significantly different (40). Collectively, these results indicate that the experiments are germane for understanding the properties of bulk water at ambient pressure.

### B. The evolution of transiently heated water versus the evolution of isothermally annealed water

An important assumption of the current experiments is that the evolution of transiently heated water versus the number of heat pulses is characteristic of the structural changes in water that is quickly brought to some temperature and then held isothermally. While we cannot provide definitive proof that this assumption holds, we can provide evidence in its favor. First, we note that for HQW films that were transiently heated to temperatures where  $f_{HQW}^{SS} \sim 0$  (e.g.  $T_{max} \sim 175$  K), the spectra after heating with many thousands of pulses are equivalent to the spectra of LDA

(i.e. a film that was never pulse-heated). For example, Figure S8 shows several spectra for HQW after transient heating to  $T_{max} = 175$  K. After  $N_p = 5 \times 10^5$ , the spectrum is very similar to LDA, which is produced by thermal annealing. So, in this case a total heating time of  $\sim 1.5$  ms at 175 K (i.e.  $\sim 5 \times 10^5$  pulses  $\cdot 3 \times 10^{-9}$  s/pulse) produces water that has the same structure as isothermally annealing water for 130 s at 135 K.

Comparison of the ice growth and nucleation rates measured via pulsed heating with previous measurements also provides support for the assumption this approach is suitable for investigating deeply supercooled water. Specifically, the growth rates of crystalline ice measured at the upper temperature limit of the pulse heating approach ( $\sim 260$  K) agreed well with the growth rates measured at the lower limit of isothermal measurements (24). Similarly, ice nucleation rates measured via pulsed-heated agree reasonably well with nucleation rates measured in rapidly cooled nanoscale water droplets (33).

### C. Nucleation rates and crystallization times in transiently heated water films

The rate of structural relaxation for supercooled water versus temperature and its relationship to the rate of ice nucleation growth are not the focus of this report. This topic, which is an important issue, will be discussed in detail in a future publication. However, in this section we briefly discuss how some aspects of the crystallization process, such as ice nucleation and growth within the transiently heated water films and the likely spatial distribution of the growing ice grains, impact the results presented in Figures 1 – 4.

First, we reiterate that the supercooled water films explored here are all metastable (or potentially unstable) with respect to crystalline ice: They all eventually crystallize as the number of heat pulses is increased. For the results presented in Figures 1, 2, 3A and 4, the crystalline ice

fraction was  $\leq 0.02$  and we argue that the ice crystallites within these films did not appreciably affect the results. However, because of the relatively large amount of water in the transiently heated films, many ice nuclei are formed on each heating pulse. To illustrate the effect of ice nucleation and growth on the current results, we consider  $T_{max} = 215$  K, which is the temperature at which the ice nucleation rate reaches a maximum –  $\tilde{J}_{max} \sim 3 \times 10^{20}$  nuclei/m<sup>3</sup>/pulse – for these pulsed-heating experiments (33). Since the volume of water,  $V_{film} = \pi r^2 \delta$  (with  $r = 3$  mm and  $\delta \sim 15$  nm), is  $\sim 4 \times 10^{-13}$  m<sup>3</sup>, we expect that  $\sim 1 \times 10^8$  ice nuclei form on each pulse. However, this amount of nucleation corresponds to a small fraction of the water: These films contain  $\sim 10^{16}$  water molecules and molecular dynamics simulations suggest that critical ice nuclei in this temperature range contain  $\sim 10^2$  molecules (12). Therefore, the fraction of the film that crystallizes is only  $\sim 10^{-6}$  per pulse at the beginning of an experiment at  $T_{max} \sim 215$  K. Fitting the relaxation of HQW at 215 K with a stretched exponential function (equation S2), gives a relaxation constant,  $N_r$ , of  $\sim 6$  pulses (see Figure S16). As a result, on the timescale for the relaxation of HQW to “steady-state” at  $T_{max} = 215$  K, the ice nuclei within the film are sparse and most of the liquid water should be unaffected by their presence.

The likely spatial distribution of ice crystallites can be demonstrated with the aid of simulations of the nucleation and growth of ice within the transiently heated water films. We have previously used a simple model of classical nucleation and growth to analyze experimental results investigating the crystallization kinetics in transiently-heated water films (33, 36). Figure S17 shows the calculated distribution of growing ice particles within a 15 nm thick water film transiently heated to  $T_{max} = 215$  K after 200 pulses. The simulation uses the previously measured nucleation and growth rates at 215 K (24, 33). The figure shows that the ice grains are sparse on the relevant length scale. For example, the blue box centered at  $(x, y) = (100$  nm, 100 nm) in the

figure shows the lateral size of a box that is 15 nm thick and contains ~32,000 water molecules (12). However, the number of water molecules in most molecular dynamics simulations that are used to investigate the properties of water are considerably less than 32,000. For example, Palmer et al. used simulations with 192, 300, 400 and 600 water molecules to demonstrate development of HDL and LDL domains with a well-defined liquid-liquid interface at the co-existence line between HDL and LDL using the ST2 water model (9). Importantly, on the timescale necessary to obtain a steady-state (metastable) structure, the vast majority of the water is far away from any ice crystallite. The data in Figure S5A support this contention where 15 temporally-identical, reversible structural transformations are observed even as the crystalline fraction approaches 10%.

*D. Comparison of the fraction of HQW in transiently-heated water films to existing estimates for the fraction of HDL-like and LDL-like species versus temperature*

In this section, we compare the steady-state fraction of HQW versus  $T_{max}$ ,  $f_{HQW}^{SS}(T_{max})$ , to existing experiments, MD simulations, and two-state models that provide information on the variation of water's structure, including the fraction of HDL-like species, versus temperature.

Because of fast structural relaxation at higher temperatures and the finite cooling rate, the current experiments are not sensitive to the structure of water at temperatures above ~ 245 K. Therefore, the infrared spectrum for HQW is representative of supercooled water. Because the temperature range for many of water's anomalous properties extend above the melting point (e.g. the temperature of maximum density for water is at 277 K), two-state models often propose that water even above the melting point is a mixture of two different structural motifs (3). Although

the structure of water at ambient temperatures is vigorously debated (4, 5, 7, 42), it would not be surprising if water at  $\sim 245$  K was a mixture of two structural motifs – HDL and LDL.

The finite cooling rate for the experiments on transiently-heated water films also influences the relationship between  $f_{HQW}^{SS}(T_{max})$  and  $f_{HDL}(T)$  for  $T_{max} < 245$  K. Once the structure has reached steady-state in a pulsed heating experiment, the structure observed after any subsequent heat pulse reflects the structure at an isothermal temperature that is somewhat less than  $T_{max}$  due to the inevitable structural relaxation during the cooling phase of every heat pulse (including the last one before an IR spectrum is obtained at low temperatures). After reaching  $T_{max}$ , the subsequent amount of structural relaxation during any given heat pulse is determined by the relaxation rate relative to the cooling rate. Because the cooling rate is largely determined by the temperature difference between  $T_{max}$  and  $T_{measure}$  and the thermal properties of the substrate, it is only weakly dependent on  $T_{max}$ . On the other hand, the relaxation rate is strongly temperature dependent (see Fig. 4b) (43). Therefore, the difference between  $f_{HQW}^{SS}(T_{max})$  and  $f_{HDL}(T)$  should decrease at lower temperatures. As a result, the midpoint for  $f_{HQW}^{SS}(T_{max})$  is expected to be lower than the corresponding midpoint for  $f_{HDL}(T)$ , i.e.  $T_0 < T_{WL}$ . For example, Fig. S12 compares the calculated inherent structure for water (13) to  $f_{HQW}^{SS}(T_{max})$ , where the experimental results have been multiplied by 0.65 to approximately match the calculations at  $\sim 210 - 220$  K. Because the effective cooling rate for the inherent structure calculations is very large, they should reflect structural changes at higher temperatures than the experiments. The red and blue dashed lines in Fig. S12 show how the results might change if larger experimental cooling rates could be realized. Presumably, the effect of the transient heating on the quenched structures could be explored with molecular dynamics simulations of the structural changes during the heat pulses.

Considerable effort has been devoted to exploring supercooled water with molecular dynamics simulations (3, 8-13, 19, 22, 31, 32, 44). Figure S10A shows the results of several MD simulations for the fraction of HDL-like molecules versus temperature compared to  $f_{HQW}^{SS}(T_{max})$  for transiently-heated water (black circles). The authors used a variety of different criteria to sort the molecules into two different categories depending on their local structures. For example, Wikfeldt, et al. used the “local structure index” (“LSI”) to classify the molecules as “low-LSI” (i.e. HDL-like, Fig. S10A, purple squares) or “high-LSI” (LDL-like) (13). Saito, et al. classified molecules as having either a “locally distorted-structure” (i.e. HDL-like, Fig. S10A, blue triangles) or “locally tetrahedral-structure” (i.e. LDL-like) (44). Moore and Molinero, (Fig. S10A, red line) (31) and Cuthbertson and Poole (Fig. S10A, orange circles) (45) both used the distance to the 5<sup>th</sup> nearest neighbor to sort molecules as either HDL-like or LDL-like. Shi, et al. (22) classified molecules according to a high-temperature disordered state, the “p state”, and a low-temperature ordered state, the “S state”, and ran simulations with both TIP5P (Fig. S10A, grey triangles) and ST2 (Fig. S10A, blue line). While all the simulations exhibit a sigmoidal dependence for the HDL-like species, the different water models and sorting criteria lead to different predicted values for (1) the fraction of HDL-like species at high temperature, (2) the mid-point of the transition from HDL-like to LDL-like species, and (3) the width of the transition.

The variety of criteria used for sorting the molecules into two groups points to the inherent uncertainty in this process when the liquid is in the single-phase region. For example, Moore and Molinero found that changing their sorting criteria (the distance to the 5<sup>th</sup> neighbor) changed the high-temperature limit for HDL-like fraction and the shape of the sigmoid, but not the mid-point (31). Therefore, to facilitate comparison of the models and the data, we have

normalized the fraction of the HDL-like component from each simulation to range from 0 to 1 (see Fig. S10B). With this rescaling, the simulations using mW water (Fig. S10B, red line) match the experimental data quite well for both the width and the mid-point of the transition from LDL-like to HDL-like species, while mid-point of the transition is higher in the other simulations.

The melting point, the temperature of maximum density,  $T_{MD}$ , and other properties for simulated water depend on the model that is used (3, 32). When Limmer and Chandler investigated the relaxation dynamics for several water models including mW, TIP4P/2005, TIP5P and ST2 (32), they found common behavior for the dynamics if the results were scaled by the  $T_{MD}$  of each model. Figure S10C shows the simulation results from Fig. S10B plotted versus the reduced temperature,  $T/T_{MD}$ . As seen in the figure, this temperature scaling also does a reasonable job of collapsing the simulations of water's structure onto a single curve. However, all the simulations predict that the mid-point of the transition is about 10% higher than the experiment: For the six simulations shown,  $0.82 \leq T_0/T_{MD} \leq 0.87$  (mean = 0.834), while  $T_0/T_{MD} = 0.76 \pm 0.014$  for the experiment. However, the midpoint for the experiments on transiently-heated water is expected to be lower than the midpoint for  $f_{HDL}(T)$  (see, for example, Fig. S12).

Various thermodynamic and dynamic properties of water versus temperature and pressure (e.g. density, isothermal compressibility, heat capacity, etc.) have been used to parameterize models for water that treat it as a non-ideal "solution" of two components (16, 46). Figure S10D (purple and orange lines) shows two examples of these models along with  $f_{HQW}^{SS}(T_{max})$ . These two models predict transitions centered at ~230 and 237 K. In two recent reports, the self-diffusivity of liquid water over a very wide temperature range was analyzed by fitting it to a mixture model in which the HDL-like and LDL-like species had their own temperature-dependent diffusivities (22, 23). The results of these models (Fig. S10D, dark and

light blue dotted lines have about the same transition temperature as  $f_{HQP}^{SS}(T_{max})$  but predicted a more gradual transition from LDL-like to HDL-like species. A similar two-state analysis of x-ray scattering data (red dotted line) placed the mid-point of the transition at 225 K (23).

For bulk supercooled water, X-ray scattering (18, 20, 34, 47), and Raman (29), Infrared (28), and x-ray spectroscopy (48) provide information on its structure to temperatures as low as 227 K. For the IR (28) and x-ray (48) spectroscopy measurements, the data only extend to 269 K and thus provide little information about the structure of deeply supercooled water (Fig. S11A, grey diamonds and squares, respectively). The decomposition of Raman spectra into two components yields an HDL fraction that decreases approximately linearly as the temperature decreases from 298 to 248 K (Fig. S11A, grey triangles) (29). As pointed out by Geissler, thermal effects will lead to apparent isosbestic points in any series of IR and Raman spectra where the measurements are made at different temperatures (30). Therefore, the extent to which the IR and Raman spectra reflect changes in the HDL-LDL composition above 245 K is an open question. However, we note that the Raman data provide no evidence for an increasing rate of change for water's structure down to 248 K, i.e. no indication that the transition out of the high temperature region, where HDL-like species are expected to dominate the structure, has begun.

X-ray scattering experiments provide the most detailed information available on the structure of bulk, supercooled water (6, 20, 34, 47-51). Isothermal measurements extend down to 244 K, while measurements on rapidly cooling water droplets reach as low as 227 K (18, 20, 52). Collectively, the data clearly show that water's structure changes as it cools, but the interpretation of those changes relative to various water models is debated (7). Nonetheless, much of the available data indicates that water's structure changes slowly with temperature above 245 K. For example, the position of the first and second sharp diffraction peaks,  $Q_1$  and

$Q_2$ , have been accurately measured down to 244 K (Fig S11B, crosses (34), squares (47)), and with lower accuracy to 227 K (Fig. S11B, triangles (18)). Both peak positions change continuously down to  $\sim 230$  K, and possibly even 227 K. Similarly, the heights of both these peaks,  $S_1$  and  $S_2$ , (Fig. 11C, blue symbols) change smoothly with temperature above 244 K (Fig. S11C, diamonds (34) and crosses (47)). Some of the x-ray data suggests the onset of more rapid changes below  $\sim 245$  K (18, 20, 52). For example, the position of the 5<sup>th</sup> peak in water's oxygen-oxygen pair distribution function,  $r_5$  increases as  $T$  decreases (Fig. S11A, blue diamonds (52)). However, at  $\sim 245$  K,  $r_5$  appears to go through a maximum (Fig. S11A, blue crosses (52)). The position of the 4<sup>th</sup> peak,  $r_4$  might decrease throughout this temperature range (Fig. S11A, red circles and triangles).  $r_4$  might decrease more quickly below 245 K (52), but the change, if any, for  $r_4$  is quite small.

Therefore, the available IR, Raman and x-ray data for bulk water all suggest that the structure of water varies slowly with temperature above  $\sim 245$  K and provide some clues that the structure is changing more quickly with temperature below that. Thus, while those data do not allow us to determine the relative amounts of HDL and LDL in HQW, it does suggest that the experiments on transiently-heated water films were sensitive to the structure in the range where it was changing the most rapidly versus temperature.

X-ray scattering experiments also provide information on the structure of LDA and high-density amorphous ice (HDA) for temperatures below 165 K (49, 50, 53). Extrapolating the available x-ray data into No-man's Land can provide some hints on the behavior of water in that region. For example, extrapolating the position of the  $Q_1$  peak suggests a crossover at  $\sim 185$  K, while it is less clear how should  $Q_2$  behave in No-man's Land (Fig. 11B). An increase in the height of the second sharp diffraction peak,  $S_2$ , is associated with increasing tetrahedrality in the

liquid (34). For LDA,  $S_2$  and  $S_1$  (Fig. S11C, blue squares, (50)) are both substantially larger than they are for water at  $\sim 245$  K, while the number of interstitial molecules ( $0.326 \text{ nm} < r < 0.396 \text{ nm}$ ) in the oxygen-oxygen pair distribution function is considerably lower for LDA (Fig. S11C, red square (50)) than for water (Fig. S11C, red crosses and diamonds (34)). The temperature dependence of these features in No-man's land is unclear.

*E. IR spectroscopy, inherent structures, and continuous versus bimodal distributions of "species"*

Our experiments use IR spectroscopy to investigate the structural changes in supercooled water as a function of  $T_{max}$ . An important observation is that IR spectra of supercooled water can be represented as a linear combination of two spectra 1) as it evolves towards its steady-state configuration at a specific  $T_{max}$ , and 2) at steady-state for a range of different maximum temperatures. However, Geissler has shown that, for liquids with inhomogeneously broadened spectra, isosbestic points will naturally appear in experiments performed at different temperatures, even if no structurally distinct species are present (30). In a related paper, Geissler and co-workers showed how this analysis can be used to explain the presence of an apparent isosbestic point in the Raman spectra of isolated HOD in water for temperatures above 273 K (5). Therefore, that analysis calls into question our interpretation of the IR spectra presented here. We will refer to this analysis below as the "Geissler Model" or GM.

The basic idea of the GM is that at different temperatures, thermal effects will typically lead to changes in inhomogeneously broadened absorption bands in liquids. However, there will always be a few frequencies where these temperature effects cancel and/or are small (30). As a result, the intensity will not change much at those points, i.e. they will look like isosbestic points.

Furthermore, this will happen even if the underlying distribution of microscopic states is continuous. Therefore, the presence of an isosbestic point is not sufficient to prove the existence of two, structurally distinct species (i.e. a discontinuous distribution of microstates). We agree with that analysis and the resulting conclusions. However, our experimental conditions are different and some of the assumptions underlying that analysis do not apply in this case.

The first, and most important distinction, is that the IR spectra were all obtained at the same temperature (70 K) for the experiments reported here. Therefore, the temperature-dependent effects arising from measurements made at different temperatures do not apply here. As an example of how the current results differ from the GM, we note that the IR spectra of LDA measured at 70 K after transient heating to  $90 \text{ K} \leq T_{max} \leq 170 \text{ K}$  do not change (see Fig. S9). If the GM applied in these experiments, we would expect to see changes in the IR spectra for such a wide range of temperatures. In contrast, the results are consistent with a two-state mixture model in which the amount of the high-temperature structural motif is expected to be very low at such low temperatures, leading to the observed temperature-independent spectra.

We agree, as discussed by Geissler (30) and Soper (7), that there will be strong thermal effects that are likely to be very important and perhaps dominate the results for measurements made at different temperatures. In particular, Geissler analyzed the results for liquid water for  $T > 273 \text{ K}$ . For that temperature range, the fraction of water expected to have the low-temperature structural motif (e.g. LDL) is small, and the temperature-related effects should be large. We also reiterate that our experiments show that there is not a discontinuous first order phase transition between LDA and HQW (or LDL and HDL) at zero pressure and low temperatures. Within the context of two-state, mixture models, the water in our experiments is always in the supercritical regime (3, 16, 46). Thus, there is no free-energy barrier separating LDA from HQW (or LDL and

HDL), and the two components do not phase separate. Instead, the results suggest water is composed of fluctuating regions which can be classified as “HDL-like” and “LDL-like.” Small angle x-ray scattering is sensitive to these fluctuations and has shown that the correlation length scale associated with these regions grows as the temperature decreases (20). Molecular dynamics simulations have identified these fluctuating “HDL-like” and “LDL-like” regions (22, 31), and also observed how the size of the “LDL-like” regions grow with decreasing temperature (31). The clustering evident in the experiments and the molecular dynamics simulations suggests that the liquid is not acting as an ideal mixture. In the two-state mixture models, the degree of non-ideality is captured in a parameter (“ $w$ ” or “ $\omega$ ”) that controls whether the system exhibits a liquid-liquid critical point (the LLC scenario) or not (the singularity-free scenario) (16, 46).

A second issue concerning the relevance of the GM to the current experiments is that it assumes that the liquid is in thermodynamic equilibrium. Therefore, it does not directly address the question of how the liquid approaches equilibrium (or metastable equilibrium for a supercooled liquid). Thus, it is not immediately obvious how to apply that analysis to our experiments where we monitor the evolution of water from an initial, non-equilibrium configuration towards its steady-state configuration at a given pulsed heating temperature. For the results shown in Figure 2, the spectra were all measured at 70 K and the pulsed heating temperature was 215 K, so the two relevant temperatures in that experiment,  $T_{max}$  and  $T_{measure}$ , did not change. The only thing that changed was the number of heat pulses. However, the resulting IR spectra did change as the structure of water evolved towards its steady-state structure at 215 K. It is noteworthy that even though  $T_{max}$  and  $T_{measure}$  did not change, the intermediate spectra could all be represented as a linear combination of the two “basis” spectra – LDA and HQW. For the data shown in Figure 4,  $f_{HQW}^{SS}(T_{max})$  was determined from individual

experiments where  $T_{max}$  and  $T_{measure}$  also did not change, but nonetheless the intermediate spectra were all reproduced by linear combinations of the LDA and HQW spectra.

Finally, we note that Ni and Skinner have calculated the IR spectra of supercooled water in the OH-stretch region as a function of temperature for several different pressures (26). At all the pressures they examined, the calculated IR spectra at different temperatures displayed an approximate isosbestic point. More importantly, they found that at any given pressure the changes in the IR spectra versus temperature became more abrupt as the pressure approached the critical pressure, and then (apparently) discontinuous when the pressure exceeded the critical pressure. These simulations suggest that even for measurements made at different temperatures in the supercooled regime, the IR spectra are reporting on changes in the liquid structure.

## Supplemental Figures:

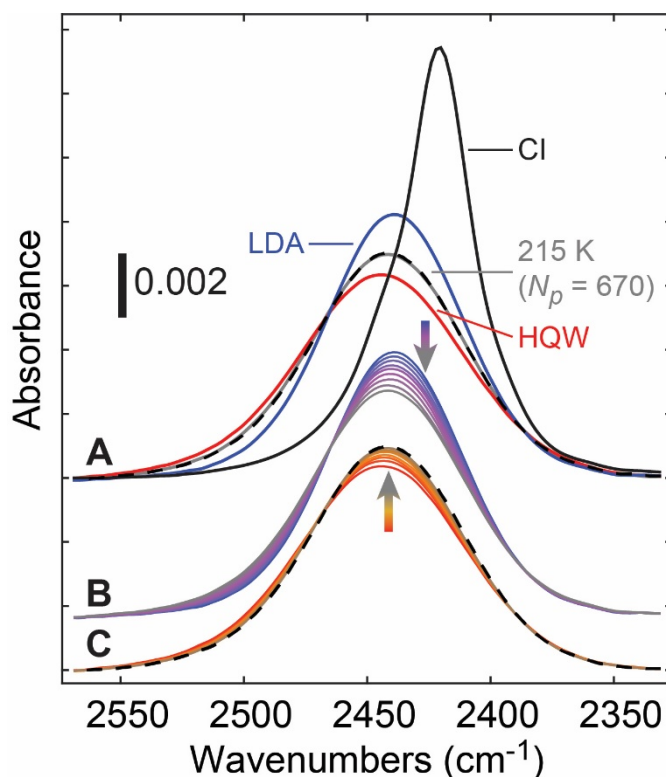


**Fig. S1.**

IR spectra in the isolated HOD stretch region. The spectra shown are the same as those in Figure 1B, but here focusing on the behavior of the isolated HOD molecules within the water (10% of the molecules are HOD). (A) The IR spectra for HQW, LDA and CI (red, blue and black lines, respectively) are all distinct. After 670 heat pulses, the resulting spectra (solid gray and dashed black lines) are independent of the initial configuration and intermediate between the spectra of hyper-quenched water and LDA. (B) LDA or (C) HQW that was heated to  $T_{max} = 215$  K evolved to the same “steady-state” structure. For  $N_p < 700$ , the fraction of crystalline ice within the films was less than 2%. Fitting the IR spectra in the isolated HOD stretch region to a linear combination of HQW, LDA and CI spectra yields results that are the same within experimental uncertainty to those shown in Figure 2.

---

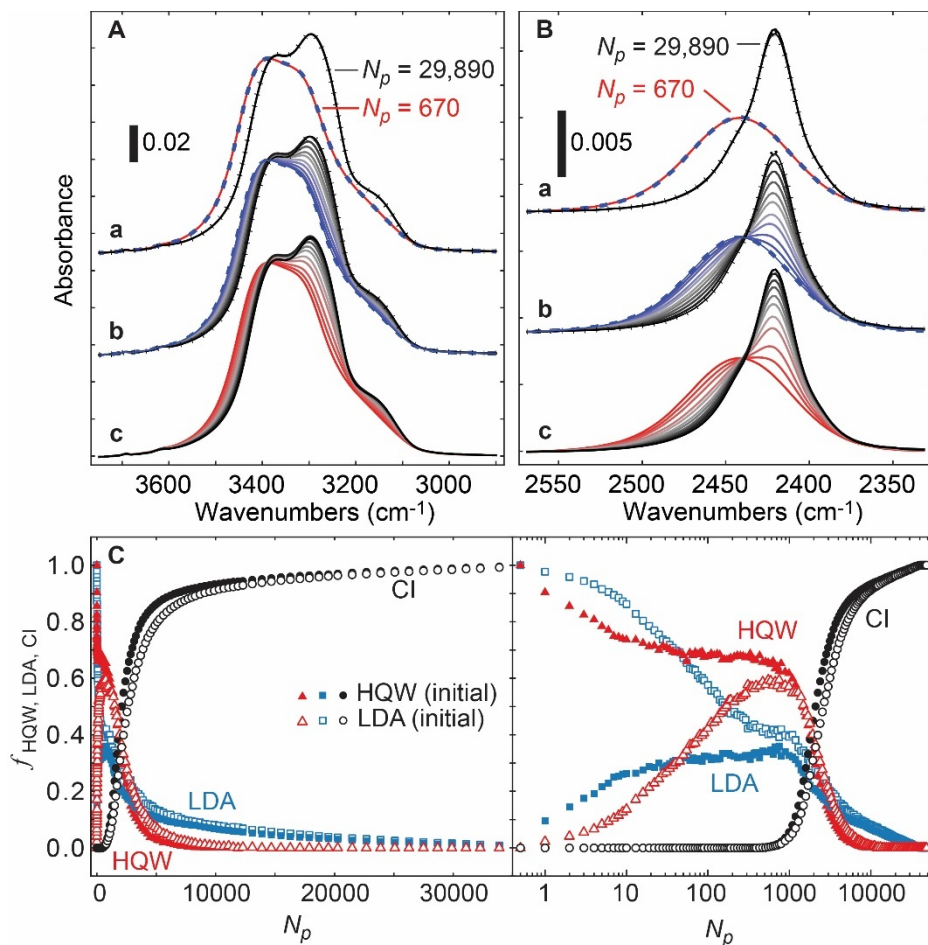


**Fig. S2.**

Crystallization of water heated to  $T_{max} = 215$  K. For the experiments shown in Figure 1, the water eventually crystallizes (i.e.  $f_{CI} > 0.02$  for  $N_p > 670$ ). Panels A and B show the corresponding IR spectra in the OH-stretch and isolated OD-stretch regions, respectively. (a): IR spectra after  $N_p = 670$  (dashed blue and solid red lines) and  $N_p = 29890$  (black line or black line with  $\times$ 's) are the same for LDA and HQW. (b) LDA and (c) HQW for  $N_p = 670, 1290, 1590, 1940, 2240, 2690, 3140, 3890, 5090, 8690$  and  $29890$ . As  $f_{CI}$  increases, the spectra redshift in both the (A) OH-stretch and (B) isolated OD-stretch regions. (C)  $f_{HQW}$ ,  $f_{LDA}$  and  $f_{CI}$  versus  $N_p$  determined from fitting the spectra to a linear combination of HQW, LDA, and CI. The left and right panels show the results versus  $N_p$  on a linear and logarithmic scale, respectively. Note that the nominal temperature was  $T_{max} = 215$  K for the experiments starting with LDA and HQW. However, for the LDA film (open symbols), the actual temperature was likely somewhat lower ( $\sim 2$  K) leading to the somewhat smaller value for  $f_{HQW}^{SS}$  and the longer time required for that film to crystallize.

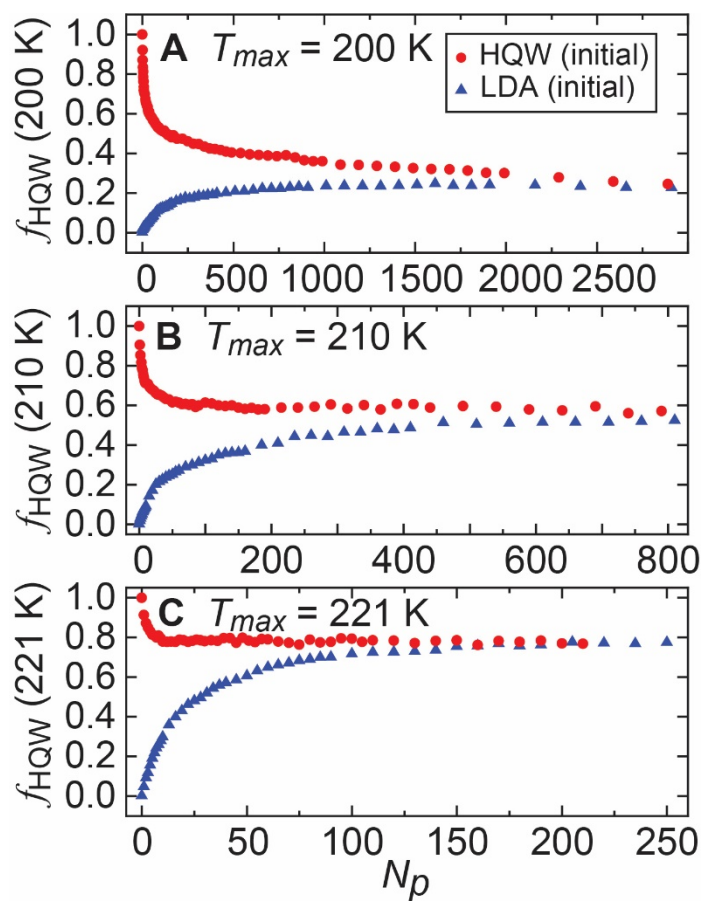


**Fig. S3.**

$f_{HQW}$  versus the number of heat pulses,  $N_p$ , for water that was transiently heated to (a)  $T_{max} = 200$  K, (b)  $T_{max} = 210$  K, (c)  $T_{max} = 221$  K. For each temperature, the relaxation kinetics were measured starting from HQW (red circles) and LDA (blue triangles). For a given  $T_{max}$ , water starting from HQW or LDA approached the same steady-state structure, although the kinetics were consistently slower when starting from LDA. In each case,  $f_{CI} \leq 0.02$  for the range shown.

---

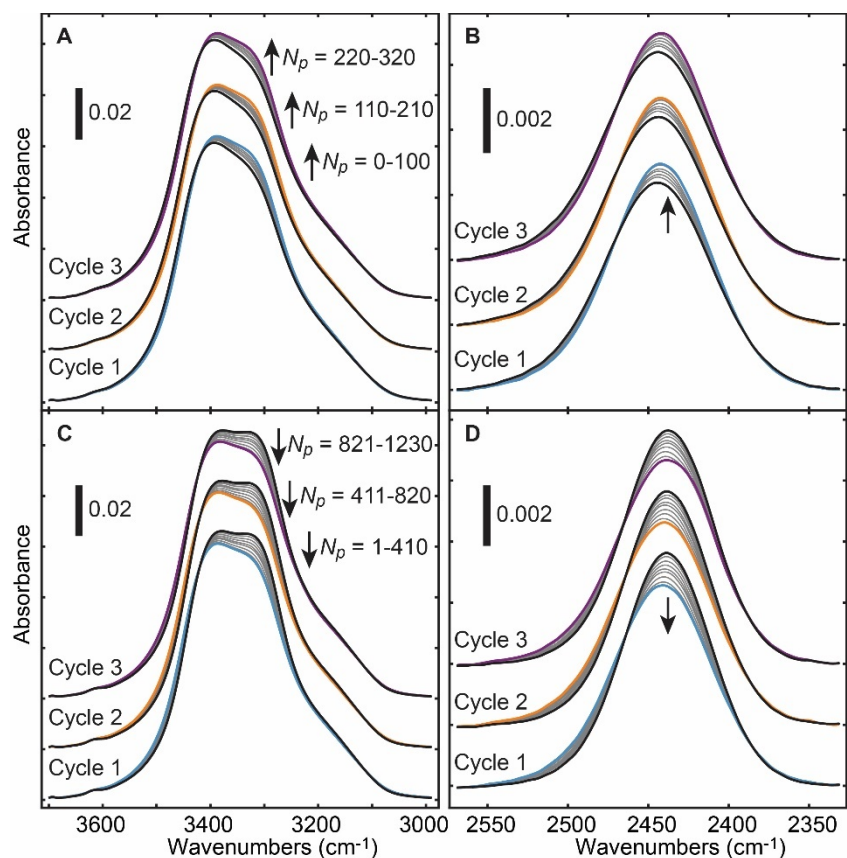


**Fig. S4.** IR spectra for the results shown in Figure 3 in the OH-stretch region (A, C) and the isolated HOD region (B, D). A, B: Starting from HQW (Cycle 1, black line), the water was heated to  $T_{max} = 215$  K (for 100 pulses) and then  $T_{max} = 252$  K (for 10 pulses). This sequence was repeated two more times (Cycles 2 and 3). The spectral changes upon heating to 215 are shown for each cycle, while the rapid conversion of the structure back to HQW upon heating to 252 K is not shown. As the number of heat pulses at 215 K increases in each cycle, the spectra change due to the increasing fraction of LDA. C, D: Starting from LDA (Cycle 1, black line), the water was heated to  $T_{max} = 215$  K (for 410 pulses). As the number of heat pulses increases, the spectra change due to the increasing fraction of HQW (Cycle 1, grey – blue lines). After 410 heat pulses, the film was heated isothermally at 135 K for 130 s and LDA was recovered (Cycle 2, black line). Pulsed heating to  $T_{max} = 215$  K a second time (Cycle 2, grey – orange lines) resulted in similar structural changes as those observed in Cycle 1. Another round of annealing at 135 K and pulsed heating to 215 K (Cycle 3, grey - purple lines) also produced similar changes. Although it is difficult to see in the spectra, the crystalline fraction has increased to  $\sim 0.01$  at the beginning of the second cycle of transient heating to 215 K.

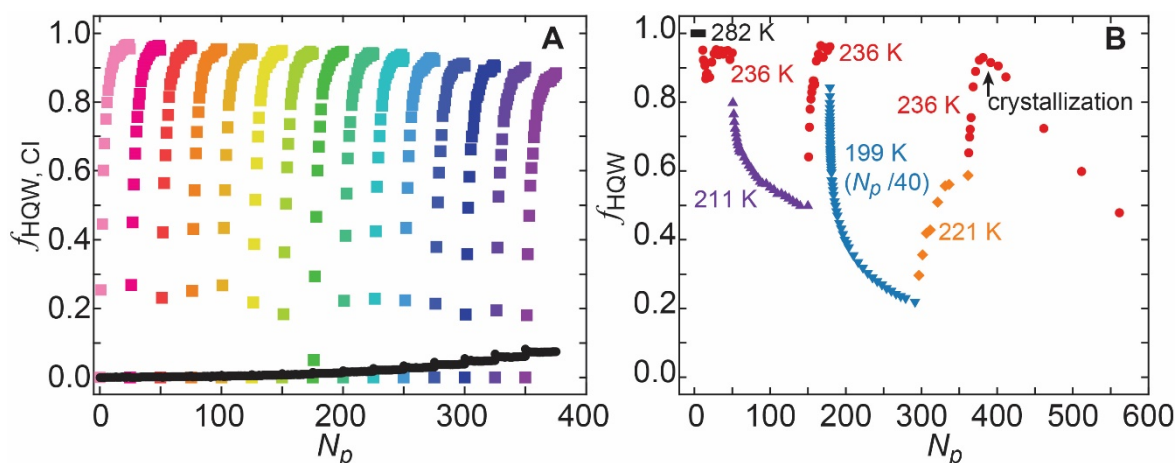


**Fig. S5.** Reversible structural changes for supercooled water. A:  $f_{HQW}$  and  $f_{CI}$  versus  $N_p$  for a water film where the temperature was cycled 15 times between  $T_{max} = 241$  K (25 heat pulses for each cycle) and isothermal annealing at 135 K for 130 s. The different colored symbols show  $f_{HQW}$  versus the total number of heat pulses. After 25 heat pulses for each cycle at  $T_{max} = 241$  K, the film was isothermally annealed at 135 K and  $f_{HQW}$  reset to zero. The black circles show  $f_{CI}$  as the (non-reversible) crystalline phase slowly grew as the experiment proceeded. Note that the structure of the liquid component continued to reversibly respond to changes in the temperature even as the crystalline component increased. B:  $f_{HQW}$  versus  $N_p$  for a water film heated to several different maximum temperatures. HQW was heated to  $T_{max} = 282$  K (black squares), 236 K (red circles), and 211 K (purple triangles). At  $T_{max} = 211$  K,  $f_{HQW}$  dropped to  $\sim 0.5$ , but the film had not reached “steady state.” Upon heating to 236 K a second time (red circles),  $f_{HQW}$  returned to  $\sim 0.95$  which was the value it had on the first cycle at 236 K. Changing  $T_{max}$  to 199 K (blue diamonds,  $N_p/40$ ), led to another decrease in  $f_{HQW}$  although at a much slower rate (note the number of pulses at 199 K has been divided by 40 in the figure). Upon increasing  $T_{max}$  to 221 K,  $f_{HQW}$  increased again (orange diamonds). Finally, during the third cycle of heating the water to 236 K (red circles), the film began to crystallize causing  $f_{HQW}$  to decrease, this time without a corresponding increase in  $f_{LDA}$  (not shown).

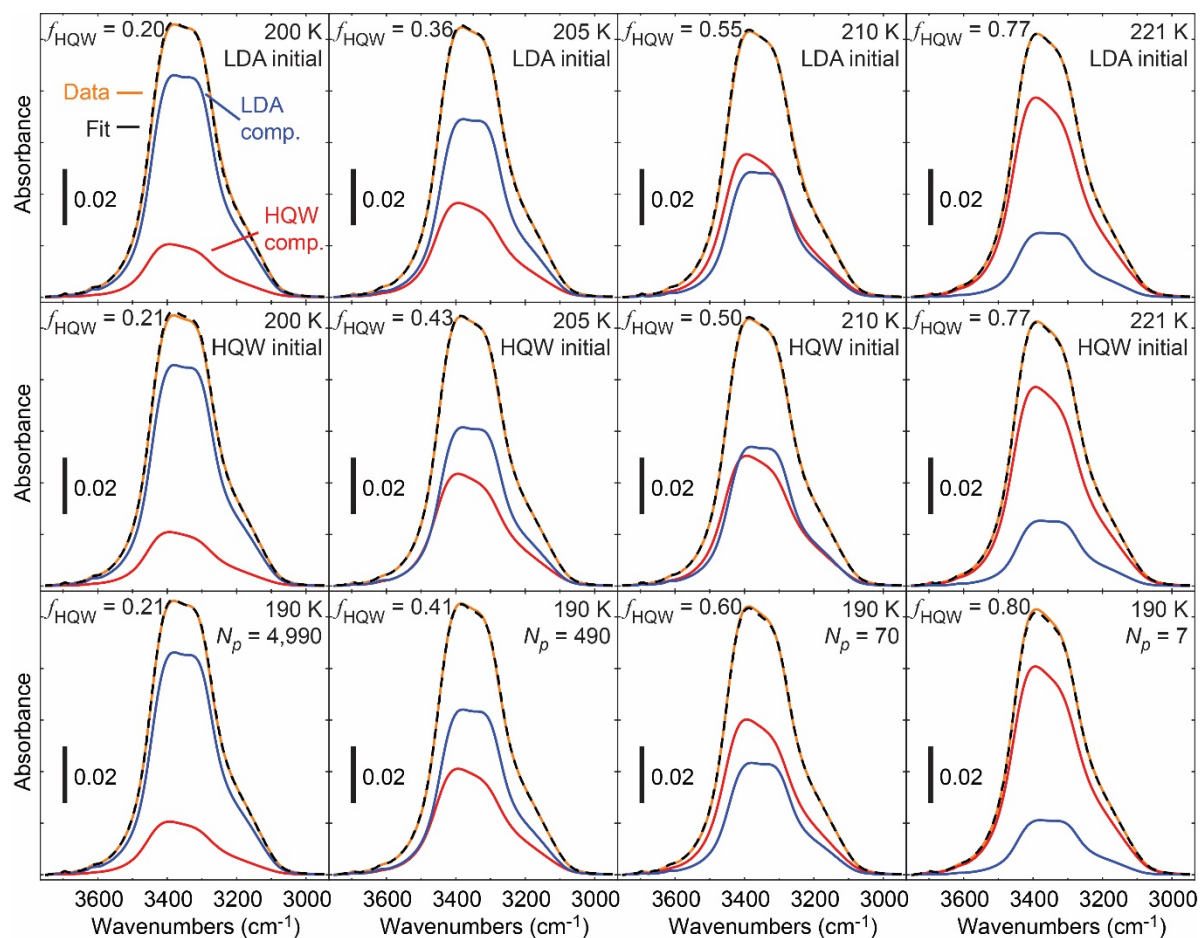


**Fig. S6.** IR spectra of  $\sim 15$  nm thick (50 ML) water films transiently heated to different temperatures and the results of fitting them to linear combinations of LDA, HQW, and CI. The orange lines show the data, the dashed black lines are the fits to the data, and the blue and red lines are the corresponding LDA and HQW components. For these results, the fraction of crystalline ice,  $f_{CI}$ , was negligible ( $\leq 0.02$ ) so it was not displayed in the figure. The top row (initial structure = HQW) and middle row (initial structure = LDA) show the steady-state spectra for water at the indicated temperatures and compositions. The structure just prior to the onset of measurable crystallization ( $f_{CI} \sim 0.02$ ) was defined as the steady-state structure. The bottom row shows the spectra for HQW that was heated to 190 K for  $N_p = 7, 70, 490$  and 4990 pulses (right to left in the figure). Because the steady-state value of  $f_{HQW}$  is  $\sim 0.06$  at 190 K (see Fig. 4), these spectra reflect the water structure prior to reaching steady-state. Generally, spectra such as these that were obtained as the film evolved towards the steady-state structure can also be fit as a linear combination of HQW and LDA.

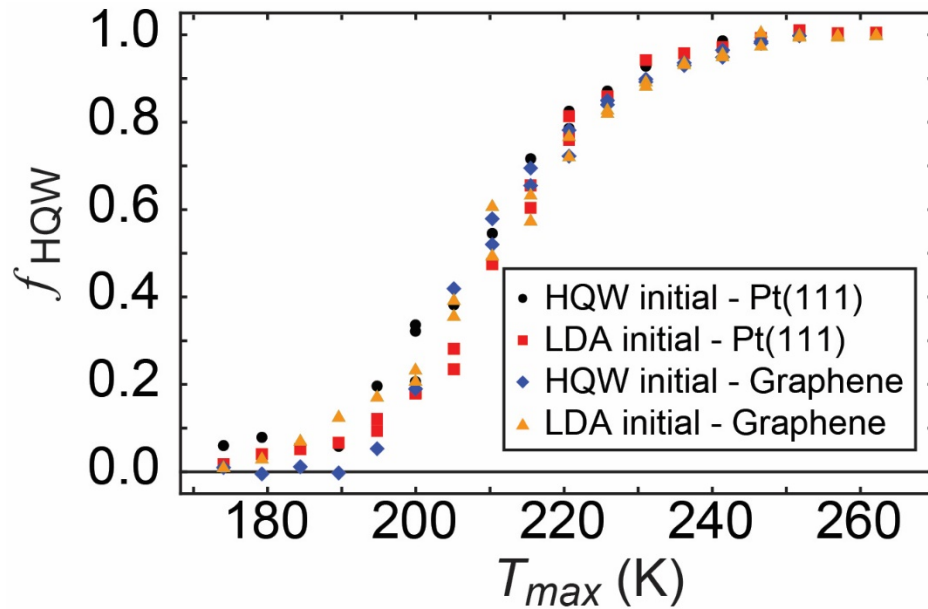


**Fig. S7.** The steady-state fraction of HQW,  $f_{HQW}$ , versus temperature. The experiments were conducted for four different configurations: (1) HQW films deposited on Pt(111) (black circles); (2) HQW films deposited on graphene/Pt(111) (blue diamonds); (3) LDA films deposited on Pt(111) (red squares); and (4) LDA films deposited on graphene/Pt(111) (orange triangles). The average of these individual experiments is reported in Figure 4 with the error bars showing the standard deviation of the individual measurements.

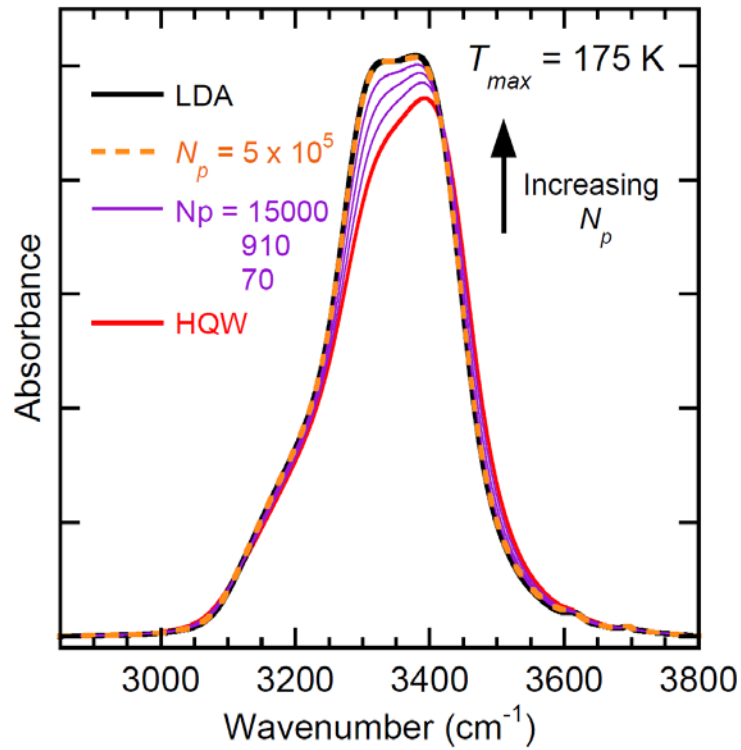


**Fig. S8.** Water IR spectra for HQW (red line) transiently heated to  $T_{max} = 175$  K for  $N_p = 70$ , 910, 15000 (purple lines) and  $5 \times 10^5$  (dashed orange line). After  $5 \times 10^5$  pulses at  $T_{max} = 175$  K, the IR spectrum is essentially indistinguishable from the spectrum of water isothermally annealed at the glass transition temperature (i.e. LDA, black line).

---

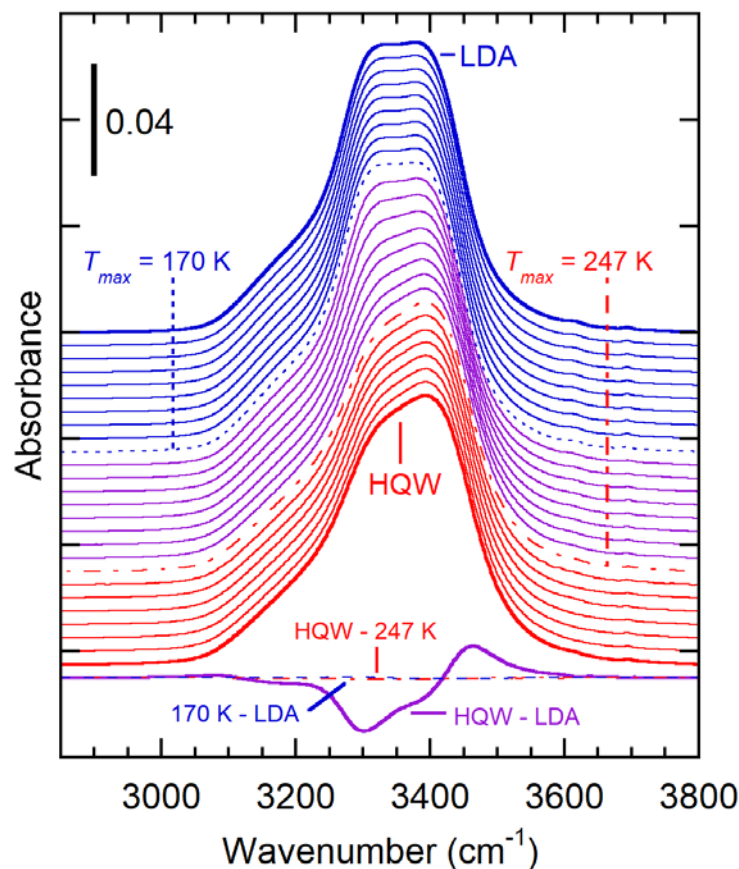


**Fig. S9.** Steady-state IR spectra of transiently heated water for  $90 \text{ K} \leq T_{max} \leq 297 \text{ K}$ . The IR spectrum for LDA, corresponding to water that was annealed at 135 K for 130 s, is also shown for reference (bold blue line). For water transiently heated to  $90 \text{ K} \leq T_{max} \leq 170 \text{ K}$  (blue lines: 90, 100, 110, 120, 130, 140, 150, 160, 170 K, top to bottom), the spectra are essentially indistinguishable from the LDA spectrum. For  $T_{max} \geq 247 \text{ K}$  (red lines: 247, 252, 257, 262, 267, 272, 282, 297 K (HQW), top to bottom), the spectra are indistinguishable from HQW (bold red line). The steady-stated IR spectra only change over a relatively narrow temperature range of  $170 \text{ K} < T_{max} < 247 \text{ K}$  (purple lines: 190, 200, 205, 210, 215, 221, 231, 241 K, top to bottom). At the bottom of the figure, difference spectrum  $\Delta S_{HQW-LDA} = S_{HQW}(\omega) - S_{LDA}(\omega)$  (purple line);  $\Delta S_{170K-LDA} = S(170 \text{ K}, \omega) - S_{LDA}(\omega)$  (dashed blue line); and  $\Delta S_{HQW-247K} = S_{HQW}(\omega) - S(247 \text{ K}, \omega)$  (dot-dash red line) show that appreciable changes in the IR spectra only occur for  $170 \text{ K} < T_{max} < 247 \text{ K}$ .

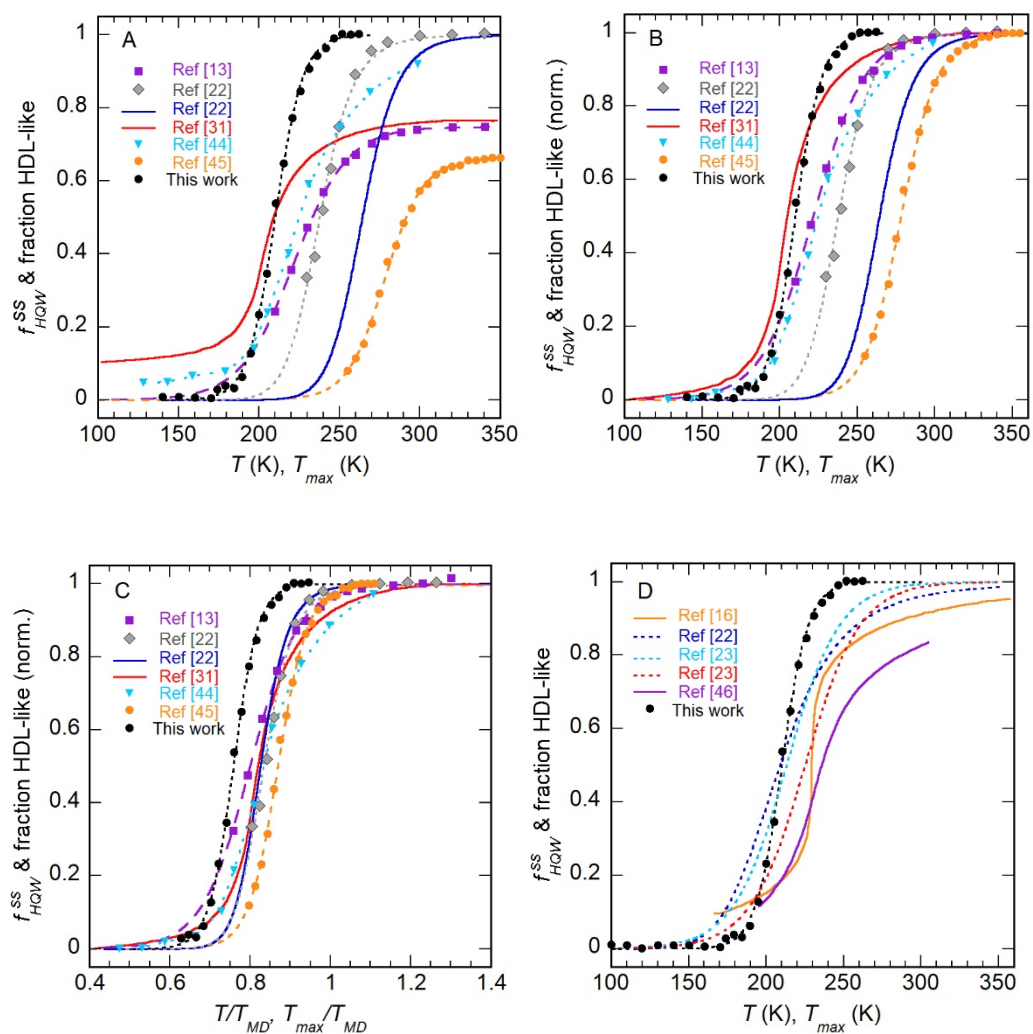


Fig. S10. Comparison of  $f_{H2O}^{SS}(T_{max})$  to previous reports for  $f_{HDL}(T)$ . (A) MD simulations have used a variety of criteria and water models (TIP4P/2005 – purple squares (13) and blue triangles (44); TIP5P – grey triangles (22); ST2 – solid blue line (22) and orange circles (45); and mW – red line (31)) to determine the fraction of HDL-like species. (B) The simulation results from (A) are shown rescaled vertically so that the fraction of HDL-like species is  $\sim 0$  at low temperatures and  $\sim 1$  at high temperatures. (C) Starting with the results from (B), the temperatures have also been normalized by the temperature of maximum density,  $T_{MD}$ , for each water model (32). (D) This panel shows the fraction of HDL-like species (as reported, i.e. without rescaling) for athermal mixture models (solid orange (15) and purple lines (46)) and two-state analyses of self-diffusion (dashed, light (23) and dark blue lines (22)) and x-ray structure (red dashed line (23)) for liquid water. See the discussion in the Supplemental Text, Section D for details.

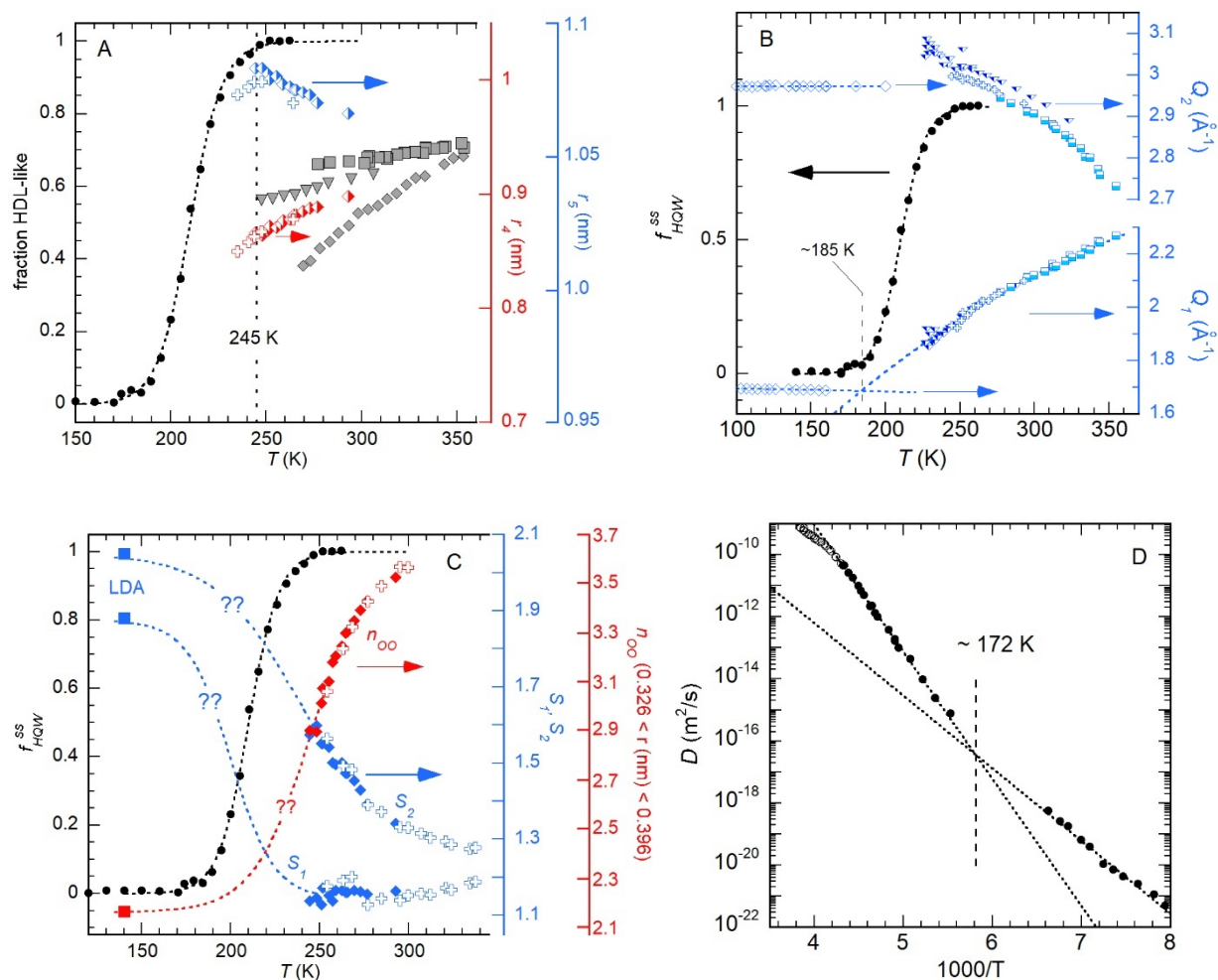
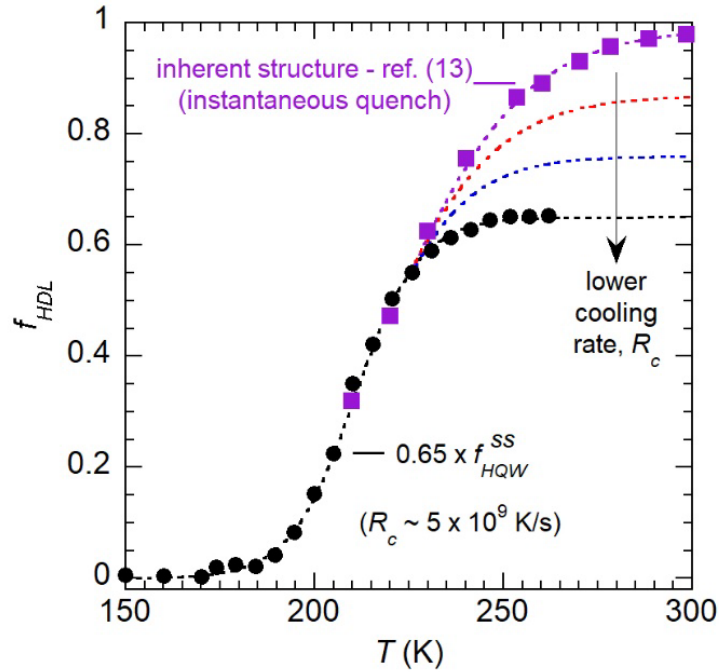
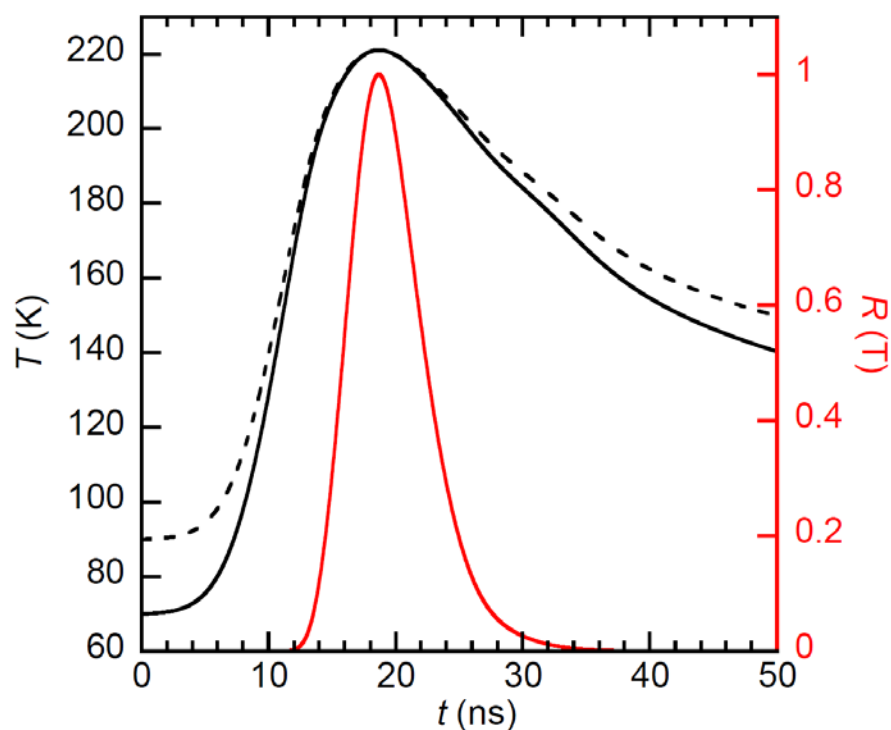


Fig. S11. Comparison of  $f_{HQW}^{ss}(T_{max})$  to other experiments. In A – C,  $f_{HQW}^{ss}(T_{max})$  from this work are shown as solid black circles and the black dashed lines are a logistic function fit. A. The fraction HDL-like species from IR (grey diamonds) (28), Raman (grey triangles) (29), and x-ray (grey squares) (48) spectroscopies. The positions of the 4<sup>th</sup> and 5<sup>th</sup> peaks in the pair distribution function,  $r_4$  (red symbols) and  $r_5$  (blue symbols), have also been measured (crosses) (52) and (half-filled diamonds) (47). B. The positions of the first and second sharp diffraction peaks (blue symbols),  $Q_1$  and  $Q_2$ , versus  $T$  (diamonds (49), triangles (18), crosses (34), squares (47)). C. The heights of the 1<sup>st</sup> and 2<sup>nd</sup> sharp diffraction peaks (blue symbols),  $S_1$  and  $S_2$ , and the number of interstitials,  $n_{oo}$ , (red symbols) for water (crosses (51) and diamonds (34)) and LDA (squares (50)). D. An Arrhenius extrapolation of the self-diffusion in water (24) suggests a crossover at  $\sim 172$  K. See the discussion in the Supplemental Text, Section D for details.



**Fig. S12.** Comparison of  $f_{HQW}^{SS}(T_{max})$  to the inherent structures of water calculated with the TIP4P/2005 water model at 1 bar (13). Here,  $f_{HQW}^{SS}(T_{max})$  was multiplied by 0.65 to match the calculation for  $T \sim 210 - 220$  K. (As discussed in the main text and the ST (section D), the composition of  $HQW$  in terms of HDL and LDL is unknown, so the appropriate scaling of  $f_{HQW}^{SS}(T_{max})$  for comparison to  $f_{HDL}(T)$  is also unknown.) The inherent structure calculations have a very high effective cooling rate,  $R_c$ . In contrast,  $R_c \sim 5 \times 10^9$  K/s for the experiments, which limits the ability to track the structural changes at higher temperatures. The red and blue dashed lines indicate how the experimental results might change if higher cooling rates could be achieved.



**Fig. S13.** Temperature and rate versus time for a transiently heated water film. The solid black line shows  $T(t)$  for a 50 ML water film with  $T_{max} = 223$  K and  $T_{measure} = 70$  K. The red line shows the (normalized) rate of a hypothetical process,  $R(t)$ , which has an Arrhenius activation energy of 0.34 eV. For any process with a rapidly increasing rate versus temperature, the majority of change during a heat pulse occurs when  $T(t)$  is within a few degrees of  $T_{max}$ . Our previous experiments were performed with  $T_{measure} = 90$  K. The dashed black line shows  $T(t)$  in that case. A lower starting temperature leads to slightly higher heating and cooling rates before and after  $T_{max}$ , respectively.

---

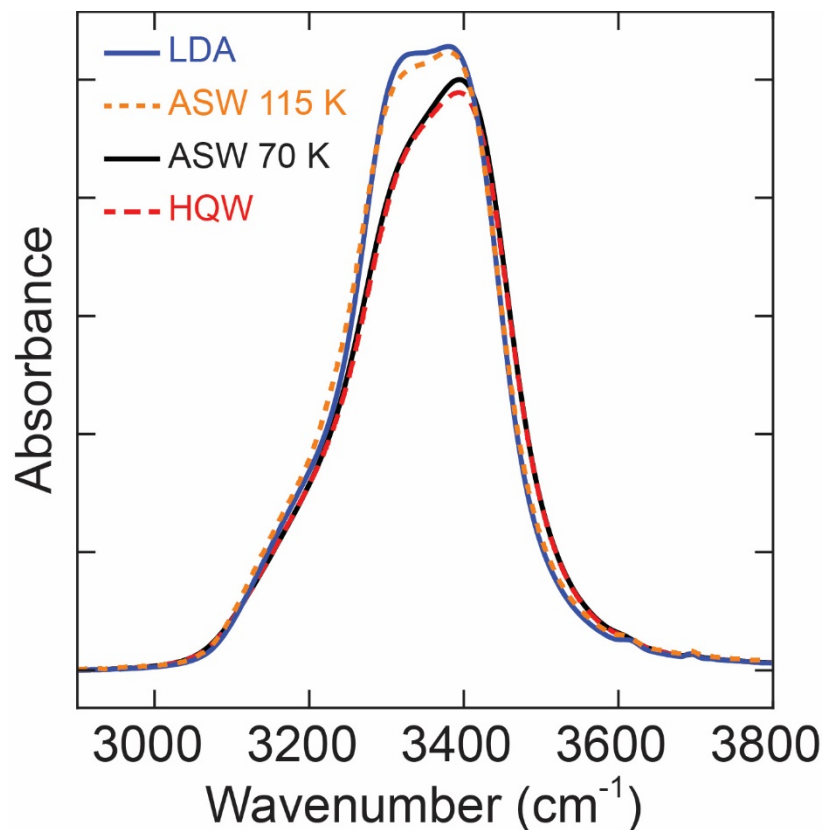


**Fig. S14.** IR spectra for LDA, HQW and amorphous solid water (ASW) films deposited at 70 K (black line) and 115 K (orange dashed line). All the IR spectra were taken at 70 K. For ASW films deposited at 70 K, the IR spectrum is similar to HQW (red dashed line). However, ASW films deposited at higher temperatures anneal as they grow to varying degrees (depending on the temperature). For example, a film deposited at 115 K is similar to LDA (solid blue line). Deposition at temperatures above 115 K led to increasing amounts of crystalline ice within the films.

---

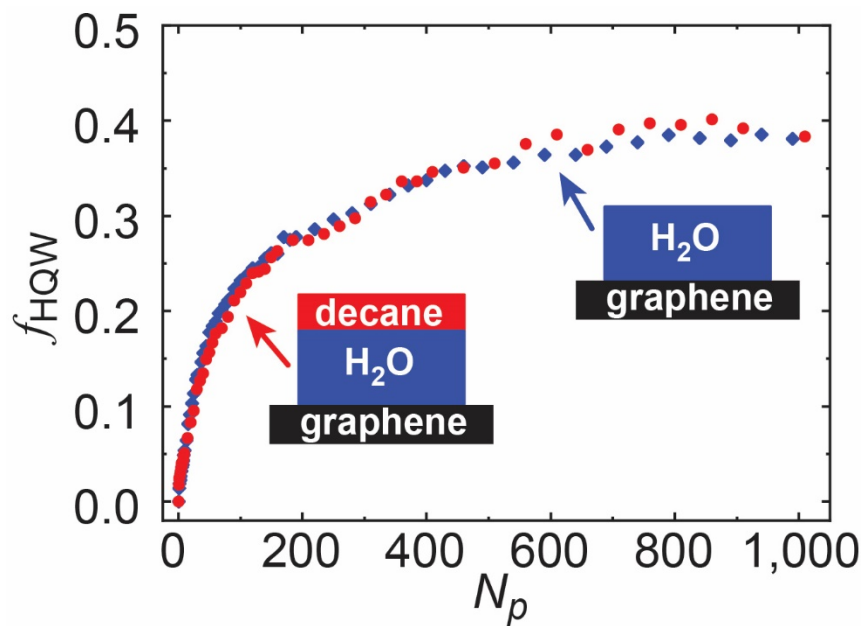


**Figure S15.**  $f_{HQW}$  versus  $N_p$  for  $T_{max} = 205$  K for a water film with and without a 20 ML decane layer adsorbed on top. Changing the outer interface for the water film did not have an appreciable effect on the relaxation kinetics or the steady-state structure.

---

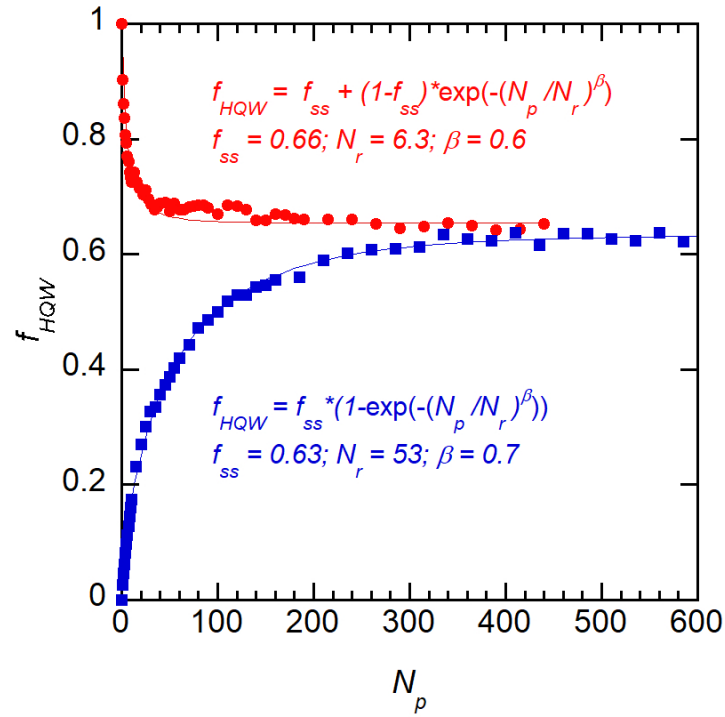


**Fig. S16.**  $f_{HQW}$  versus the number of heat pulses,  $N_p$  for  $T_{max} = 215$  K starting from HQW (red circles) or LDA (blue squares). The solid lines show fits to the data with stretched exponential functions. The characteristic relaxation constants,  $N_r$ , are  $\sim 6$  and  $53$  pulses when starting from HQW and LDA, respectively.

---

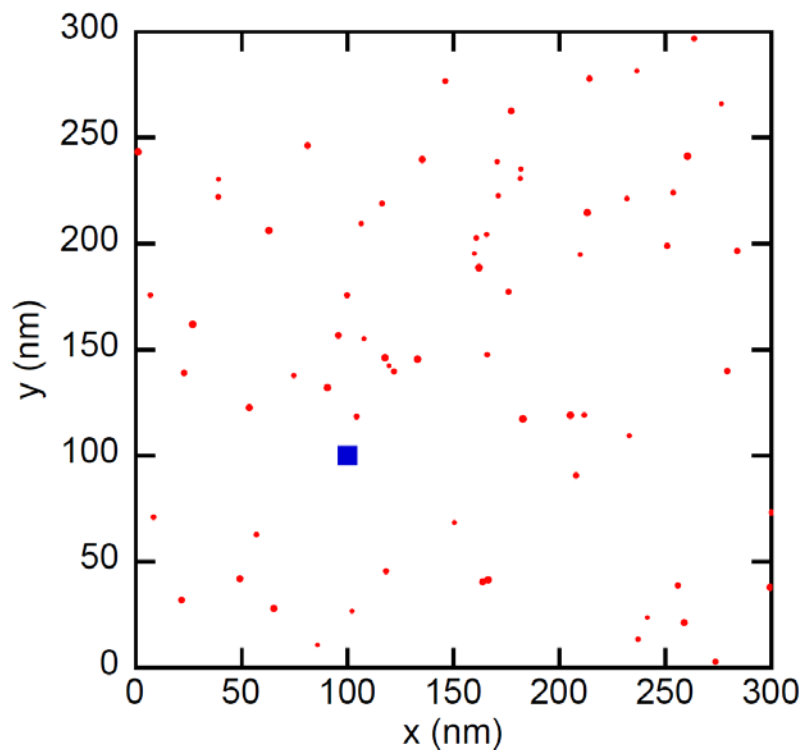


**Fig. S17.** Crystallization simulation for  $T_{max} = 215$  K. The red dots show the locations (projected onto the x-y plane) and approximate sizes of the ice crystallites in a portion of a 50 ML ( $\Delta z = 15$  nm thick) water film after 200 pulses. For comparison, the blue box shows the size of a box containing  $\sim 32,000$  molecules. At  $T_{max} = 215$  K, the ice nucleation and growth rates are  $\tilde{J}(T_{max}) \sim 3 \times 10^{20}$  nuclei/m<sup>3</sup>/pulse and  $\tilde{G}(T_{max}) = 4.4 \times 10^{-3}$  nm/pulse, respectively.

---

## References and Notes

1. R. J. Speedy, Stability-limit conjecture. An interpretation of the properties of water. *J. Chem. Phys.* **86**, 982–991 (1982). [doi:10.1021/j100395a030](https://doi.org/10.1021/j100395a030)
2. O. Mishima, H. E. Stanley, The relationship between liquid, supercooled and glassy water. *Nature* **396**, 329–335 (1998). [doi:10.1038/24540](https://doi.org/10.1038/24540)
3. P. Gallo, K. Amann-Winkel, C. A. Angell, M. A. Anisimov, F. Caupin, C. Chakravarty, E. Lascaris, T. Loerting, A. Z. Panagiotopoulos, J. Russo, J. A. Sellberg, H. E. Stanley, H. Tanaka, C. Vega, L. Xu, L. G. M. Pettersson, Water: A Tale of two liquids. *Chem. Rev.* **116**, 7463–7500 (2016). [doi:10.1021/acs.chemrev.5b00750](https://doi.org/10.1021/acs.chemrev.5b00750) [Medline](#)
4. F. H. Stillinger, Water revisited. *Science* **209**, 451–457 (1980). [doi:10.1126/science.209.4455.451](https://doi.org/10.1126/science.209.4455.451) [Medline](#)
5. J. D. Smith, C. D. Cappa, K. R. Wilson, R. C. Cohen, P. L. Geissler, R. J. Saykally, Unified description of temperature-dependent hydrogen-bond rearrangements in liquid water. *Proc. Natl. Acad. Sci. U.S.A.* **102**, 14171–14174 (2005). [doi:10.1073/pnas.0506899102](https://doi.org/10.1073/pnas.0506899102) [Medline](#)
6. A. Nilsson, L. G. M. Pettersson, The structural origin of anomalous properties of liquid water. *Nat. Commun.* **6**, 8998 (2015). [doi:10.1038/ncomms9998](https://doi.org/10.1038/ncomms9998) [Medline](#)
7. A. K. Soper, Is water one liquid or two? *J. Chem. Phys.* **150**, 234503 (2019). [doi:10.1063/1.5096460](https://doi.org/10.1063/1.5096460) [Medline](#)
8. P. H. Poole, F. Sciortino, U. Essmann, H. E. Stanley, Phase behavior of metastable water. *Nature* **360**, 324–328 (1992). [doi:10.1038/360324a0](https://doi.org/10.1038/360324a0)
9. J. C. Palmer, F. Martelli, Y. Liu, R. Car, A. Z. Panagiotopoulos, P. G. Debenedetti, Metastable liquid-liquid transition in a molecular model of water. *Nature* **510**, 385–388 (2014). [doi:10.1038/nature13405](https://doi.org/10.1038/nature13405) [Medline](#)
10. S. Sastry, P. G. Debenedetti, F. Sciortino, H. E. Stanley, Singularity-free interpretation of the thermodynamics of supercooled water. *Phys. Rev. E* **53**, 6144–6154 (1996). [doi:10.1103/PhysRevE.53.6144](https://doi.org/10.1103/PhysRevE.53.6144) [Medline](#)
11. D. T. Limmer, D. Chandler, The putative liquid-liquid transition is a liquid-solid transition in atomistic models of water. *J. Chem. Phys.* **135**, 134503 (2011). [doi:10.1063/1.3643333](https://doi.org/10.1063/1.3643333) [Medline](#)
12. E. B. Moore, V. Molinero, Structural transformation in supercooled water controls the crystallization rate of ice. *Nature* **479**, 506–508 (2011). [doi:10.1038/nature10586](https://doi.org/10.1038/nature10586) [Medline](#)
13. K. T. Wikfeldt, A. Nilsson, L. G. M. Pettersson, Spatially inhomogeneous bimodal inherent structure of simulated liquid water. *Phys. Chem. Chem. Phys.* **13**, 19918–19924 (2011). [doi:10.1039/c1cp22076d](https://doi.org/10.1039/c1cp22076d) [Medline](#)
14. L. Xu, P. Kumar, S. V. Buldyrev, S.-H. Chen, P. H. Poole, F. Sciortino, H. E. Stanley, Relation between the Widom line and the dynamic crossover in systems with a liquid-liquid phase transition. *Proc. Natl. Acad. Sci. U.S.A.* **102**, 16558–16562 (2005). [doi:10.1073/pnas.0507870102](https://doi.org/10.1073/pnas.0507870102) [Medline](#)

15. F. Mallamace, M. Broccio, C. Corsaro, A. Faraone, D. Majolino, V. Venuti, L. Liu, C.-Y. Mou, S.-H. Chen, Evidence of the existence of the low-density liquid phase in supercooled, confined water. *Proc. Natl. Acad. Sci. U.S.A.* **104**, 424–428 (2007). [doi:10.1073/pnas.0607138104](https://doi.org/10.1073/pnas.0607138104) [Medline](#)
16. V. Holten, M. A. Anisimov, Entropy-driven liquid-liquid separation in supercooled water. *Sci. Rep.* **2**, 713 (2012). [doi:10.1038/srep00713](https://doi.org/10.1038/srep00713) [Medline](#)
17. A. Taschin, P. Bartolini, R. Eramo, R. Righini, R. Torre, Evidence of two distinct local structures of water from ambient to supercooled conditions. *Nat. Commun.* **4**, 2401 (2013). [doi:10.1038/ncomms3401](https://doi.org/10.1038/ncomms3401) [Medline](#)
18. J. A. Sellberg, C. Huang, T. A. McQueen, N. D. Loh, H. Laksmono, D. Schlesinger, R. G. Sierra, D. Nordlund, C. Y. Hampton, D. Starodub, D. P. DePonte, M. Beye, C. Chen, A. V. Martin, A. Barty, K. T. Wikfeldt, T. M. Weiss, C. Caronna, J. Feldkamp, L. B. Skinner, M. M. Seibert, M. Messerschmidt, G. J. Williams, S. Boutet, L. G. M. Pettersson, M. J. Bogan, A. Nilsson, Ultrafast X-ray probing of water structure below the homogeneous ice nucleation temperature. *Nature* **510**, 381–384 (2014). [doi:10.1038/nature13266](https://doi.org/10.1038/nature13266) [Medline](#)
19. J. Russo, H. Tanaka, Understanding water's anomalies with locally favoured structures. *Nat. Commun.* **5**, 3556 (2014). [doi:10.1038/ncomms4556](https://doi.org/10.1038/ncomms4556) [Medline](#)
20. K. H. Kim, A. Späh, H. Pathak, F. Perakis, D. Mariedahl, K. Amann-Winkel, J. A. Sellberg, J. H. Lee, S. Kim, J. Park, K. H. Nam, T. Katayama, A. Nilsson, Maxima in the thermodynamic response and correlation functions of deeply supercooled water. *Science* **358**, 1589–1593 (2017). [doi:10.1126/science.aap8269](https://doi.org/10.1126/science.aap8269) [Medline](#)
21. L. P. Singh, B. Issenmann, F. Caupin, Pressure dependence of viscosity in supercooled water and a unified approach for thermodynamic and dynamic anomalies of water. *Proc. Natl. Acad. Sci. U.S.A.* **114**, 4312–4317 (2017). [doi:10.1073/pnas.1619501114](https://doi.org/10.1073/pnas.1619501114) [Medline](#)
22. R. Shi, J. Russo, H. Tanaka, Origin of the emergent fragile-to-strong transition in supercooled water. *Proc. Natl. Acad. Sci. U.S.A.* **115**, 9444–9449 (2018). [doi:10.1073/pnas.1807821115](https://doi.org/10.1073/pnas.1807821115) [Medline](#)
23. N. J. Hestand, J. L. Skinner, Perspective: Crossing the Widom line in no man's land: Experiments, simulations, and the location of the liquid-liquid critical point in supercooled water. *J. Chem. Phys.* **149**, 140901 (2018). [doi:10.1063/1.5046687](https://doi.org/10.1063/1.5046687) [Medline](#)
24. Y. Xu, N. G. Petrik, R. S. Smith, B. D. Kay, G. A. Kimmel, Growth rate of crystalline ice and the diffusivity of supercooled water from 126 to 262 K. *Proc. Natl. Acad. Sci. U.S.A.* **113**, 14921–14925 (2016). [doi:10.1073/pnas.1611395114](https://doi.org/10.1073/pnas.1611395114) [Medline](#)
25. Materials and methods are available as supplementary materials.
26. Y. Ni, J. L. Skinner, IR spectra of water droplets in no man's land and the location of the liquid-liquid critical point. *J. Chem. Phys.* **145**, 124509 (2016). [doi:10.1063/1.4963736](https://doi.org/10.1063/1.4963736) [Medline](#)
27. B. M. Auer, J. L. Skinner, IR and Raman spectra of liquid water: Theory and interpretation. *J. Chem. Phys.* **128**, 224511 (2008). [doi:10.1063/1.2925258](https://doi.org/10.1063/1.2925258) [Medline](#)

28. Y. Maréchal, The molecular structure of liquid water delivered by absorption spectroscopy in the whole IR region completed with thermodynamics data. *J. Mol. Struct.* **1004**, 146–155 (2011). [doi:10.1016/j.molstruc.2011.07.054](https://doi.org/10.1016/j.molstruc.2011.07.054)
29. Q. Sun, Local statistical interpretation for water structure. *Chem. Phys. Lett.* **568-569**, 90–94 (2013). [doi:10.1016/j.cplett.2013.03.065](https://doi.org/10.1016/j.cplett.2013.03.065)
30. P. L. Geissler, Temperature dependence of inhomogeneous broadening: On the meaning of isosbestic points. *J. Am. Chem. Soc.* **127**, 14930–14935 (2005). [doi:10.1021/ja0545214](https://doi.org/10.1021/ja0545214) [Medline](#)
31. E. B. Moore, V. Molinero, Growing correlation length in supercooled water. *J. Chem. Phys.* **130**, 244505 (2009). [doi:10.1063/1.3158470](https://doi.org/10.1063/1.3158470) [Medline](#)
32. D. T. Limmer, D. Chandler, Corresponding states for mesostructure and dynamics of supercooled water. *Faraday Discuss.* **167**, 485–498 (2013). [doi:10.1039/c3fd00076a](https://doi.org/10.1039/c3fd00076a) [Medline](#)
33. G. A. Kimmel, Y. Xu, A. Brumberg, N. G. Petrik, R. S. Smith, B. D. Kay, Homogeneous ice nucleation rates and crystallization kinetics in transiently-heated, supercooled water films from 188 K to 230 K. *J. Chem. Phys.* **150**, 204509 (2019). [doi:10.1063/1.5100147](https://doi.org/10.1063/1.5100147) [Medline](#)
34. C. Benmore, L. C. Gallington, E. Soignard, Intermediate range order in supercooled water. *Mol. Phys.* **117**, 2470–2476 (2019). [doi:10.1080/00268976.2019.1567853](https://doi.org/10.1080/00268976.2019.1567853)
35. Y. Xu, C. J. Dibble, N. G. Petrik, R. S. Smith, A. G. Joly, R. G. Tonkyn, B. D. Kay, G. A. Kimmel, A nanosecond pulsed laser heating system for studying liquid and supercooled liquid films in ultrahigh vacuum. *J. Chem. Phys.* **144**, 164201 (2016). [doi:10.1063/1.4947304](https://doi.org/10.1063/1.4947304) [Medline](#)
36. Y. Xu, N. G. Petrik, R. S. Smith, B. D. Kay, G. A. Kimmel, Homogeneous nucleation of ice in transiently-heated, supercooled liquid water films. *J. Phys. Chem. Lett.* **8**, 5736–5743 (2017). [doi:10.1021/acs.jpcllett.7b02685](https://doi.org/10.1021/acs.jpcllett.7b02685) [Medline](#)
37. K. S. Kjær, T. B. van Driel, J. Kehres, K. Haldrup, D. Khakhulin, K. Bechgaard, M. Cammarata, M. Wulff, T. J. Sørensen, M. M. Nielsen, Introducing a standard method for experimental determination of the solvent response in laser pump, x-ray probe time-resolved wide-angle x-ray scattering experiments on systems in solution. *Phys. Chem. Chem. Phys.* **15**, 15003–15016 (2013). [doi:10.1039/C3CP50751C](https://doi.org/10.1039/C3CP50751C) [Medline](#)
38. L. Cheng, P. Fenter, K. L. Nagy, M. L. Schlegel, N. C. Sturchio, Molecular-scale density oscillations in water adjacent to a mica surface. *Phys. Rev. Lett.* **87**, 156103 (2001). [doi:10.1103/PhysRevLett.87.156103](https://doi.org/10.1103/PhysRevLett.87.156103) [Medline](#)
39. G. Cicero, J. C. Grossman, E. Schwegler, F. Gygi, G. Galli, Water confined in nanotubes and between graphene sheets: A first principle study. *J. Am. Chem. Soc.* **130**, 1871–1878 (2008). [doi:10.1021/ja074418+](https://doi.org/10.1021/ja074418+) [Medline](#)
40. B. V. Derjaguin, Y. I. Rabinovich, N. V. Churaev, Direct measurement of molecular forces. *Nature* **272**, 313–318 (1978). [doi:10.1038/272313a0](https://doi.org/10.1038/272313a0)

41. H. Hu, Y. Sun, Molecular dynamics simulations of disjoining pressure effect in ultra-thin water film on a metal surface. *Appl. Phys. Lett.* **103**, 263110 (2013).  
[doi:10.1063/1.4858469](https://doi.org/10.1063/1.4858469)
42. J. Niskanen, M. Fondell, C. J. Sahle, S. Eckert, R. M. Jay, K. Gilmore, A. Pietzsch, M. Dantz, X. Lu, D. E. McNally, T. Schmitt, V. Vaz da Cruz, V. Kimberg, F. Gel'mukhanov, A. Föhlisch, Compatibility of quantitative x-ray spectroscopy with continuous distribution models of water at ambient conditions. *Proc. Natl. Acad. Sci. U.S.A.* **116**, 4058–4063 (2019). [doi:10.1073/pnas.1815701116](https://doi.org/10.1073/pnas.1815701116) [Medline](#)
43. S. Cervený, F. Mallamace, J. Swenson, M. Vogel, L. Xu, Confined water as model of supercooled water. *Chem. Rev.* **116**, 7608–7625 (2016).  
[doi:10.1021/acs.chemrev.5b00609](https://doi.org/10.1021/acs.chemrev.5b00609) [Medline](#)
44. S. Saito, B. Bagchi, I. Ohmine, Crucial role of fragmented and isolated defects in persistent relaxation of deeply supercooled water. *J. Chem. Phys.* **149**, 124504 (2018).  
[doi:10.1063/1.5044458](https://doi.org/10.1063/1.5044458) [Medline](#)
45. M. J. Cuthbertson, P. H. Poole, Mixturelike behavior near a liquid-liquid phase transition in simulations of supercooled water. *Phys. Rev. Lett.* **106**, 115706 (2011).  
[doi:10.1103/PhysRevLett.106.115706](https://doi.org/10.1103/PhysRevLett.106.115706) [Medline](#)
46. F. Caupin, M. A. Anisimov, Thermodynamics of supercooled and stretched water: Unifying two-structure description and liquid-vapor spinodal. *J. Chem. Phys.* **151**, 034503 (2019).  
[doi:10.1063/1.5100228](https://doi.org/10.1063/1.5100228) [Medline](#)
47. L. B. Skinner, C. J. Benmore, J. C. Neufeind, J. B. Parise, The structure of water around the compressibility minimum. *J. Chem. Phys.* **141**, 214507 (2014). [doi:10.1063/1.4902412](https://doi.org/10.1063/1.4902412)  
[Medline](#)
48. C. Huang, K. T. Wikfeldt, T. Tokushima, D. Nordlund, Y. Harada, U. Bergmann, M. Niebuhr, T. M. Weiss, Y. Horikawa, M. Leetmaa, M. P. Ljungberg, O. Takahashi, A. Lenz, L. Ojamäe, A. P. Lyubartsev, S. Shin, L. G. M. Pettersson, A. Nilsson, The inhomogeneous structure of water at ambient conditions. *Proc. Natl. Acad. Sci. U.S.A.* **106**, 15214–15218 (2009). [doi:10.1073/pnas.0904743106](https://doi.org/10.1073/pnas.0904743106) [Medline](#)
49. C. Lin, J. S. Smith, S. V. Sinogeikin, G. Shen, Experimental evidence of low-density liquid water upon rapid decompression. *Proc. Natl. Acad. Sci. U.S.A.* **115**, 2010–2015 (2018).  
[doi:10.1073/pnas.1716310115](https://doi.org/10.1073/pnas.1716310115) [Medline](#)
50. D. Mariedahl, F. Perakis, A. Späh, H. Pathak, K. H. Kim, G. Camisasca, D. Schlesinger, C. Benmore, L. G. M. Pettersson, A. Nilsson, K. Amann-Winkel, X-ray scattering and O-O pair-distribution functions of amorphous ices. *J. Phys. Chem. B* **122**, 7616–7624 (2018).  
[doi:10.1021/acs.jpcc.8b04823](https://doi.org/10.1021/acs.jpcc.8b04823) [Medline](#)
51. L. B. Skinner, C. Huang, D. Schlesinger, L. G. M. Pettersson, A. Nilsson, C. J. Benmore, Benchmark oxygen-oxygen pair-distribution function of ambient water from x-ray diffraction measurements with a wide Q-range. *J. Chem. Phys.* **138**, 074506 (2013).  
[doi:10.1063/1.4790861](https://doi.org/10.1063/1.4790861) [Medline](#)
52. H. Pathak, A. Späh, K. H. Kim, I. Tsironi, D. Mariedahl, M. Blanco, S. Huotari, V. Honkimäki, A. Nilsson, Intermediate range O-O correlations in supercooled water down to 235 K. *J. Chem. Phys.* **150**, 224506 (2019). [doi:10.1063/1.5100811](https://doi.org/10.1063/1.5100811) [Medline](#)

53. M. C. Bellissent-Funel, L. Bosio, A. Hallbrucker, E. Mayer, R. Sridi-Dorbez, X-ray and neutron scattering studies of the structure of hyperquenched glassy water. *J. Chem. Phys.* **97**, 1282–1286 (1992). [doi:10.1063/1.463254](https://doi.org/10.1063/1.463254)